LASER INDUCED GRATINGS IN
STRONTIUM BARIUM NIOBATE

By

SCOTT A. HOLMSTROM

Bachelor of Science
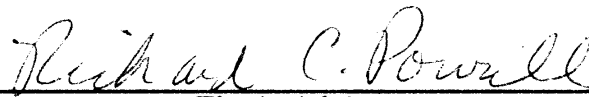
Southwest Missouri State University
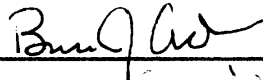
Springfield, Missouri

1990

Submitted to the Faculty of the
Graduate College of the
Oklahoma State University
in partial fulfillment of
the requirements for
the Degree of
MASTER OF SCIENCE
December, 1993

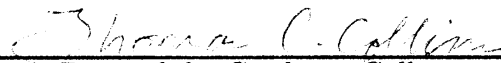LASER INDUCED GRATINGS IN
STRONTIUM BARIUM NIOBATE

Thesis Approved:

Richard C. Powell
Thesis Adviser

Bruce Ackerson

Xincheng Xie

Thomas C. Collins
Dean of the Graduate College

ACKNOWLEDGMENTS

TABLE OF CONTENTS

LIST OF FIGURES

CHAPTER I

INTRODUCTION

During the past decade there has been a great deal of research done on studying processes by which light can be controlled by light. The motivation behind this is that the fastest rate a which information can be transfered is by utalizing light as its carrier. Optical fiber communications systems have been developed and installed throughout the world to aid in high speed, high volume information transfer. The work presented here studies a fundamental aspect of the control of light by light: Optical diffraction via nondegenerate four wave mixing (FWM).

Optical diffraction is achieved by interfering two light waves in a material producing a modulation in its optical properties. This harmonic modulation produces a holographic diffraction grating. A third wave is then passed through the material and, by diffraction from the grating, a fourth wave is produced. Lasers are ideally suited for the generation of gratings because they produce coherent, collimated, and intense beams which provide strong interference patterns.

The particular material that was investigated for this work, strontium barium niobate, has been extensively studied for applications in optical storage and processing in the continuous wave (cw) laser regime[1-3]. The purpose here is to extend the investigations to include experiments that use short duration (picosecond and subpicosecond), high intensity laser pulses. This type of work has been of intense interest recently because of the desire to find optical materials that have fast response times. The nonlinear optical responses to short laser pulses have previously been reported in photorefractive materials such as $Bi_{12}SiO_{20}[36,4-9]$, $Bi_{12}GeO_{20}[9]$, $BaTiO_3[10,11]$, $KNbO_3$ [12], $LiNbO_3[13]$, and $KTa_xNb_{1-x}O_3[14]$ using nanosecond and picosecond laser sources. The time scales for the electrooptic

1

signals in these crystals range from less than 100 ps for $BaTiO_3$ up to 1 ms for $KNbO_3$.

For insulating crystals under low intensity, cw, visible light illumination the donor levels in the band gap of the material are important because they are the principle means of interaction between the crystal and the light. These levels are also responsible for providing the mobile charge carriers needed for the photore-fractive effect. These band gap states are not the only mechanism for free carrier production in the short laser pulse regime. Direct band-to-band transitions become possible by multiphoton absorption when very intense light is used. This process produces an electron in the conduction band as well as a hole in the valence band, both of which are, in general, mobile. Most likely these 'extra' carriers will greatly effect the transient dynamics of any process that relies of the production of free carriers, e.g. the photorefractive effect.

CHAPTER II

THEORETICAL BACKGROUND

Crystal Properties

$Sr_xBa_{1-x}Nb_2O_6$, $0.75 \leq x \leq 0.25$, referred to as strontium barium niobate (SBN:100x), belongs to the tungsten bronze crystal family even though the limiting cases of $SrNb_2O_6$ and $BaNb_2O_6$ do not. For the mixed ferroelectric crystal, SBN, it has been found that the congruent melting composition is that with x=0.60, SBN:60[15]. Both iron-doped and nominally undoped SBN:60 were used in the experiments discussed in the chapters to follow. The optical quality single crystals were grown using the Czochralski technique at Rockwell International Science Center. The iron concentration for the doped crystal was 0.012 weight percent and it is expected that iron is present in both its Fe^{2+} and Fe^{3+} charge states. An automatic diameter control unit was used in the growth of the iron doped samples to obtain striation free crystals. The dimension of the samples were $5.0 \times 5.7 \times 5.7$ mm^3 and $5.9 \times 6.1 \times 6.1$ mm^3 for the undoped and iron doped respectively.

The tetragonal tungsten bronze crystal composition can be represented by the general formula $(A1)_4(A2)_2B_{10}O_{30}$, where A1, A2, and B are the 15-, 12-, and 6-fold coordinate sites in the crystal lattice structure. For SBN, Sr^{2+} and Ba^{2+} occupy both the 15- and 12-fold sites, however, all of the sites are not occupied so the structure is referred to as open tungsten bronze. This open structure allows for dopant ions to be easily incorporated in the crystal in order to tailor the optical properties to meet specific needs. A complete discussion of the tungsten bronze-type crystal structure can be found in a paper by Jamison.[16]

As will be discussed in chapter to follow, an important crystal property parameter used in describing the photorefractive effect are the linear electrooptic tensor elements. These elements are proportionality constants that relate an applied electric field intensity to changes in the local (region where the field is non-zero) index of refraction. A complete explanation of the electrooptic effect can be found in reference [37]. The point group symmetry of SBN is $4mm$. For crystals of this point group the electrooptic tensor has the form such that there are three independent nonzero moduli: $r_{13} = r_{23}$, $r_{42} = r_{51}$, and r_{33}. The largest of which, in SBN:60, is r_{33}. In order to enhance the electrooptic effect in SBN crystals they are poled by first being heated above the ferroelectric phase transition temperature (Curie point) and then being cooled to room temperature with an applied dc electric field of less than 10 kV.[17] Typical reported values for the electrooptic tensor elements are found in the photorefractive theory section of this thesis.

The samples must be poled because in ferroelectric crystals different regions, referred to as domains, may have the spontaneous polarization associated with ferroelectricity pointing in one of several directions. In an as-grown crystal, the multidomain state that is produced has no net polarization. Because of this, the crystals show very small, if any, piezoelectric, pyroelectric, or electrooptic effects. These effects depend on the direction of polarization and are therefore averaged out in a multidomain crystal. The poling process creates a single domain crystal thereby enhancing polarization dependent effects.

Photorefractive Effect

The photorefractive effect was first noticed in the 1960's at Bell laboratories in $LiNbO_3$ and $LiTaO_3$ crystals[18]. At the time it was referred to as optical damage because the laser light induced small changes in the local index of refraction of the crystals. These changes ruined the phase matching condition for second harmonic generation which was the subject of the original work.

In the late 1960's this damage effect was realized to have applications in optical data storage by Chen and co-workers[19]. This practical application provided

a drive for fundamental research of the photorefractive effect over the ensuing decade. Many small breakthroughs were made including the understanding of the importance of an applied electric field[20], the effects of including dopant ions in the crystals[21], contributions from the bulk photovoltaic effect[22], and, perhaps the most important, the suggestion of degenerate four wave mixing (FWM) for phase conjugation[23]. As it was first explained, this is the interaction of an arbitrary wavefront with counterpropagating plane waves in a nonlinear optical medium. These waves interact in the photorefractive material to produce a forth wave which is the complex conjugate of the original arbitrary wavefront.

In 1979, Kukhtarev et. al.[24] published a model that explained much of the phenomena that had been observed until that time. The steady state predictions of the their theory have been supported by experiments over the past 14 years and it still remains the basis for the understanding of the photorefractive effect. An overview of this band transport model is presented here to provide a basic understanding of the concepts.

The light-induced changes in the local index of refraction in electrooptic crystals are brought about by the spatial modulation of photoinduced currents by non-uniform illumination. The basic idea is that free charge carriers are produced (electrons in the conduction band and/or holes in the valence band) in the regions of the crystal that are illuminated. In the usual explanation of the photorefractive effect these free carriers are generated by the photoexcitation of impurity or dopant ion sites in the crystal. However, there may also be a contribution to the free carrier population by a multiphoton process that allows for direct band-to-band transitions. This will be discussed in the experimental chapter. Following the excitation, the charge carriers move to different regions of the crystal where they may be retrapped. Under continuous wave (cw) illumination the photoexcited charges will be reexcited and retrapped until they are moved out of the illuminated region and are trapped there. The result is ionized traps in the bright regions of the sample and filled traps in the dark regions. This amounts to an excess, in comparison to equilibrium conditions, of charge in the dark regions and a lack

of charge in the bright regions. There is an electric field associated with this nonuniform charge distribution that is referred to as a space-charge field (E_{sc}). An electric field in an electrooptic crystal yields a local change in the index of refraction. A discussion of this effect is found later in this chapter.

The remaining portion of this chapter will deal with the actual model first presented by Kukhtarev *et. al.* and will basically follow a review article by P. Gunter and J.-P. Huignard[26].

It is important to note from the start that the model is generally presented for an isotropic material illuminated by two plane waves that are unaffected by the material. In actuality most experiments deal with anisotropic materials, non-plane waves, and there is always an affect on the the light by the material. However, the simplicity that the above assumptions add to the theory outweighs the small corrections that would need be made.

There are three mechanisms for free carrier movement responsible for the photorefractive effect: diffusion, drift, and the photovoltaic effect. For particular crystals and specific experimental conditions any of the above transport processes can dominate, however in general all must be considered.

Periodic excitation arising from the interference of two beams gives rise to a spatially periodic electron distribution in the conduction band. Since there are regions of high electron density and low electron density and since conduction electrons are free to move in the crystal it can be seen that random movement will tend to 'wash out' the distribution. Electrons from high density regions will move to the low density regions. This process is referred to as diffusion. It is assumed, in the original theory, that the majority of free electrons were produced by the ionization of defects or impurities in the crystal. These donor sites are relatively stationary in the crystal so it can be seen that a charge separation, between the electrons in low density regions and their original ionized donors, is formed. This gives rise to a space-charge field that limits further smoothing of the periodic density distribution. In the limiting case that the space-charge field did not form, the density distribution would be completely smoothed. This, of course,

is not the case so what we have is a space-charge limited diffusion in experimental application. This is accounted for in the model. The diffusion contribution leading to charge separation is only important for high frequency spatial modulation of the density distribution.

The displacement of the electron distribution, as well as the ionized donor distribution, as a whole by an external field is referred to as drift. This affect can be achieved by evaporating electrodes on the faces of the crystal then applying a potential difference between them. This process enhances the photorefractive effect only if the field is applied either parallel or antiparallel to the grating/interference pattern wavevector. The grating/interference pattern wavevector is defined using the line that bisects the angle between the two beams forming the pattern. It is in the plane of the two beams and perpendicular to the bisector. The electron density distribution may also drift due to a potential difference between the crystal faces even in the absence of electrodes[25]. Indeed the zero field case is not observed experimentally unless a reverse bias field is applied to counteract the field due to the faces.

Some crystals have a polar axis associated with them, which means that in a particular direction there is a spontaneous internal electric field due specifically to the positions of the atoms that make up the crystal. The center of positive charge does not coincide with the center of negative charge. The internal electric field allows for free charge transport as well as ionic motion. The current associated with this motion is called the photovoltaic current. The total photovoltaic current density, j^{ph}, due to electronic and ionic motion is described using the photovoltaic tensor.

$$j^{ph} = \beta_{ijk} E_j E_k^* \tag{1}$$

where E_j, E_k are the electric field strengths of the 'writing' beams and β_{ijk} is the third rank photovoltaic tensor[27-29,22]. The photovoltaic tensor elements are all zero for crystals displaying a center of symmetry.

For an explanation of the photovoltaic effect as due to asymmetric charge transfer processes and Frank-Condon ionic shifts see the paper by Glass *et. al.*[22].

In general, all the above mentioned transport processes contribute to a current density given by

$$j(z,t) = e\mu n(z,t)\left[E_{sc}(z,t) - \frac{V}{L}\right] - \mu k_B T \frac{dn(z,t)}{dz} + eL_{ph}\frac{n_1(z,t)}{dt} \qquad (2)$$

when the excitation yields a grating wavevector along the polar z-axis of the crystal. In Eq. 2, V is the externally applied voltage between the two faces, L is the electrode spacing, μ is the mobility of charge carriers, k_B is Boltzmans constant, T is the temperature in Kelvin, E_{sc} is the electric field due to charge separation along the z-axis, L_{ph} is a mean effective drift length along the polar axis, n(z,t) is the total concentration of charge carriers, and $n_1(z,t)$ is the charge concentration due only to illumination.

The first two terms in Eq. 2 account for drift and diffusion and the last one accounts for the photovoltaic effect. The last term is written differently than in Eq. 1. It is an equivalent expression in that it describes the total photovoltaic current but it is written in terms of the theory developed in reference [22].

The time rate of change of the total electron concentration, n(z,t), due to the ionization of donors, charge transport and trapping is governed by the continuity equation:

$$\frac{\partial}{\partial t}n(z,t) = \frac{\partial}{\partial t}N_D^i(z,t) - \frac{1}{e}\frac{\partial}{\partial z}j(z,t) \qquad (3)$$

with the time rate of change of the ionized donor concentration, N_D^i, being

$$\frac{\partial}{\partial t}N_D^i(z,t) = [sI(z,t) + \beta]\left[N(z,t) - N_D^i(z,t)\right] - \gamma_R n(z,t)N_D^i(z,t) \qquad (4)$$

where N is the total concentration of donors. γ_R is the recombination constant, β is the rate of thermal excitation and s is the cross section of photoionization.

In the preceding paragraph, and in what is to follow, it is assumed that the material has single types of donor and trap centers. A number of papers have considered multiple donor and trap sites and their effects on the photorefractive effect. An example is a paper by LeSaux and Brun[36].

A forth equation used by Kuktarev *et. al.* in explaining the photorefractive effect is arrived at using Gauss's law.

$$\frac{\partial}{\partial z} E = \frac{4\pi e}{\epsilon} \left(n + N_A - N_D^i \right) \tag{5}$$

Where e is the charge on the electron, ϵ is the static dielectric constant, and N_A is the number density of ions that compensate for the number of ionized donors sites in the crystal under dark conditions. N_A is a constant of the crystal. These 'acceptor' sites do not take part in the photoexcitation process.

It should be noted that, in general D, μ, and ϵ are tensors and N_D and N_A could vary with position. For simplicity, however, the tensors are usually, at least initially, treated as scalars and the number densities, N_D and N_A, are assumed constant throughout the material.

The preceding four coupled equations are fundamental in describing the photorefractive effect. Given them, the task then becomes solving for the space-charge field in the crystal under specific experimental conditions. This field can then be used to calculate the temporal and spatial evolution of the index of refraction using the theory of the electrooptic effect.

Kuktarev initially solved the equations in the steady state case of cw illumination and the results have been used to explain experimental observations with great success. For the experiments presented in this thesis, cw illumination was not used. The gratings were written using a laser pulse whose duration is much shorter than the characteristic times associated with charge transport and trapping. In this case the steady state conditions do not apply. In 1983, Valley presented solutions to Kuktarevs equations for the case in which the writing beams are obtained from short-pulsed, high-irradiance lasers[30]. He presented two cases: 1) The time for recombination of carriers with ions is much less that the pulse length of the laser (quasi-cw); and 2) the recombination, drift and diffusion times are all much longer than the pulse length. An overview of the latter will be presented here. In Valley's work, only two of the charge transport processes, drift and diffusion, were considered important even though he applies his theory to a ferroelectric crystal,

BaTiO$_3$, which is known to have a spontaneous internal electric field. This omission must be because of the increased computational difficulties introduced when including the $\frac{d}{dt}n_1$ term in the current density equation.

With the omission of the photovoltaic current density term and combining the applied field, $\frac{V}{L}$, and the space-charge field, E_{sc}, into a total electric field, E, Kuktarev's equations are written

$$\frac{\partial}{\partial t}n - \frac{\partial}{\partial t}N_D^i = -\frac{1}{e}\frac{\partial}{\partial z}j \tag{6}$$

$$\frac{\partial}{\partial t}N_D^i = sI(N_D - N_D^i) - \gamma_R n N_D^i \tag{7}$$

$$j = e\mu n E - k_B T\mu\frac{\partial}{\partial z}n \tag{8}$$

$$\frac{\partial}{\partial z}E = \frac{4\pi e}{\epsilon}\left(n + N_A - N_D^i\right). \tag{9}$$

A technique in solving the equations to describe the photorefractive effect is called linearization in the grating modulation. Solutions of the above four equations are assumed to be

$$n = n_0 + \delta n(z,t) \tag{10}$$

$$N_D^i = N_{D_0}^i(t) + \delta N_D^i(z,t) \tag{11}$$

$$E = E_0 + \delta E(z,t) \tag{12}$$

$$j = j_0 + \delta j(z,t) \tag{13}$$

where the δ quantities are the terms that describe the grating. Also a form for the intensity, I, is assumed to be

$$I = I_0 + \delta I(z,t) \tag{14}$$

where $\delta I(z,t) = mI_0 e^{ik_g z}$. m is the modulation index given by

$$m = 2\frac{(I_{+1}I_{-1})^{\frac{1}{2}}}{I_{+1} + I_{-1}}\cos(2\theta p) \tag{15}$$

where $I_{\pm 1}$ is the intensity of one of the beams used in writing the grating, θ is the half-angle between them as measured inside the crystal, k_g is the grating wavenumber given by $k_g = 4\pi\sin(\theta)/\lambda$, and p=0 for light polarized perpendicular to the

plane of incidence whereas p=1 for polarization directions within the plane of incidence.

Plugging in the assumed solutions and eliminating the zeroth-order current density, electric field, and ion number density yields the equation for mean carrier number density:

$$\frac{d}{dt}n_0 = sI_0(N_D - N_A - n_0) - \gamma_R n_0(N_A - n_0).$$ (16)

The linearized equations for the δ-terms are

$$\frac{\partial}{\partial t}\delta n - \frac{\partial}{\partial t}\delta N_D^i = -\mu E_0\frac{\partial}{\partial z}\delta n - \mu n_0\frac{\partial}{\partial z}\delta E + \frac{k_B T\mu}{e}\frac{\partial^2}{\partial z^2}\delta n$$ (17)

$$\frac{\partial}{\partial t}\delta N_D^i = -sI_0\delta N_D^i + s\delta I(N_D - N_A - n_0) - \gamma_R n_0(\delta N_D^i + \delta n) - \gamma_R N_A\delta n$$ (18)

$$\frac{\partial}{\partial z}\delta E = \frac{4\pi e}{\epsilon}(\delta n - \delta N_D^i).$$ (19)

Eq. 16 is solved for a rectangular pulse of length τ_p and intensity I_0 to yield

$$n_0(t) = \frac{n_+n_-N_A\left[1 - e^{\left[-\frac{(n_+-n_-)t}{\tau_R}\right]}\right]}{n_- - n_+e^{\left[-\frac{(n_+-n_-)t}{\tau_R}\right]}}, 0 \le t \le \tau_p$$ (20)

and

$$n_0(t) = \frac{n_0(\tau_p)e^{\left[-\frac{(t-\tau_p)}{\tau_R}\right]}}{1 + \frac{n_0(\tau_p)}{N_A}\left\{1 - e^{\left[-\frac{(t-\tau_p)}{\tau_R}\right]}\right\}}, t > \tau_p,$$ (21)

Where

$$n_\pm = \frac{1}{2}\left\{-(1 + f) \pm \left[(1 + f)^2 + 4f(r - 1)\right]^{\frac{1}{2}}\right\}$$ (22)

$$\tau_R = \frac{1}{\gamma_R N_A}$$ (23)

$$r = \frac{N_D}{N_A}$$ (24)

$$f = \frac{sI_0}{\gamma_R N_A}.$$ (25)

For very high intensities the mean carrier number density saturates to N_D-N_A, which is the maximum number of carriers able to be excited from that type of site. In the limit that $\tau_p \ll \tau_R$ then

$$n_0(\tau_p) = sI_0\tau_p(N_D - N_A)$$ (26)

which is simply the total number density of carriers ionized by the pulse. This makes sense because for $\tau_p \ll \tau_R$ no carriers have had time to recombine in the time scale of the pulse.

Eq. 20 describing the carrier number density build-up as a function of time before the end of the pulse is plotted in Figure 1. $\frac{N_D}{N_A}$ and $sI_0\tau_R$ are treated as parameters. After the duration of the pulse, the carrier number density decays exponentially characteristic of the recombination time if the saturation effects in the denominator of Eq. 21 are small.

Manipulation of Eq.'s 17-19 yields a differential equation in the space-charge field given by

$$\frac{\partial^2}{\partial t^2}\delta E + \left(\frac{i}{\tau_E} + \frac{1}{\tau_D} + \frac{1}{\tau_R} + \gamma_R n_0(t) + \frac{n_0(t)}{n_0(\tau_p)\tau_{di}(\tau_p)}\right)\frac{\partial}{\partial t}\delta E$$
$$+ \left(\frac{i}{\tau_E} + \frac{1}{\tau_p}\right)\gamma_R n_0(t)\delta E = 0 \qquad (27)$$

where

$$\tau_{di}(t) = \frac{\epsilon}{4\pi e \mu n_0(t)} \qquad (28)$$

$$\tau_E = \frac{1}{k_g \mu E_0} \qquad (29)$$

$$\tau_D = \frac{e}{\mu k_B T k_g^2}. \qquad (30)$$

τ_{di} is the dielectric relaxation time, τ_E is the mean drift time, and τ_D is the diffusion time before recombination.

In general, Eq. 27 requires a numerical solution unless certain experimental conditions allow for its simplification. Its solution yields an equation describing the time dependence of the space-charge field. With this the time dependence of the index grating can be calculated using the theory of the electrooptic effect. An overview of this theory, following Yariv[37], will be presented here.

$$\frac{x^2}{n_x^2} + \frac{y^2}{n_y^2} + \frac{z^2}{n_z^2} = 1 \qquad (31)$$

This is the equation of an ellipsoid with major axes parallel to the x, y, and z directions each with length $2n_x$, $2n_y$, and $2n_z$ respectively. This equation is called the index ellipsoid where n_x, n_y, and n_z are the respective indices of refraction
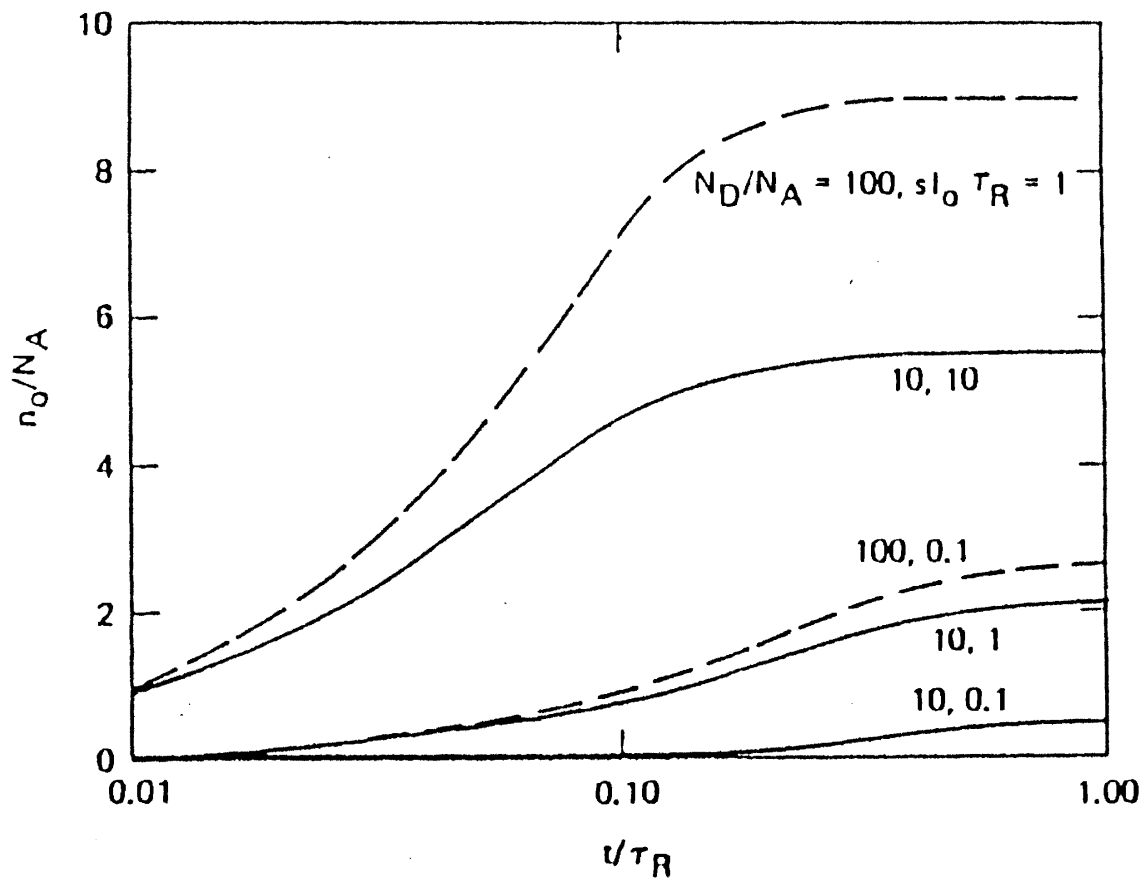
Figure 1. Carrier number density in units of trap density as a function of time t
in units of recombination time. [29]

of the crystal. Eq. 31 is used to find the two indices of refraction and the two corresponding directions of the electric displacement vector, **D**, associated with the two independent plane waves that can propagate in the crystal[37]. If these two directions have different indices of refraction this is the familiar condition known as birefringence. These waves with orthogonal polarizations and differing indices are referred to as 'ordinary' and 'extraordinary'.

The linear electrooptic effect is a change in the indices that is caused by the application of an electric field. The index ellipsoid in the presence of an electric field becomes

$$\left(\frac{1}{n^2}\right)_1 x^2 + \left(\frac{1}{n^2}\right)_2 y^2 + \left(\frac{1}{n^2}\right)_3 z^2 + \left(\frac{1}{n^2}\right)_4 yz + \left(\frac{1}{n^2}\right)_5 xz + \left(\frac{1}{n^2}\right)_6 xy = 1. \quad (32)$$

This equation must reduce to the zero-field case of Eq. 31 so,

$$\left(\frac{1}{n^2}\right)_{1,E=0} = \frac{1}{n_x^2} \; ; \; \left(\frac{1}{n^2}\right)_{2,E=0} = \frac{1}{n_y^2} \; ; \; \left(\frac{1}{n^2}\right)_{3,E=0} = \frac{1}{n_z^2} \quad (33)$$

$$\left(\frac{1}{n^2}\right)_{4,5,6,E=0} = 0.$$

The linear change in the coefficients of Eq. 32 due to an arbitrary electric field , **E**, is defined as

$$\Delta \left(\frac{1}{n^2}\right)_i = \sum_{j=1}^{3} r_{ij} E_j \quad (34)$$

In the summation over j, $1 \leftrightarrow x$, $2 \leftrightarrow y$, and $3 \leftrightarrow z$. This equation can be expressed in matrix form as

$$\begin{bmatrix} \Delta \left(\frac{1}{n^2}\right)_1 \\ \Delta \left(\frac{1}{n^2}\right)_2 \\ \Delta \left(\frac{1}{n^2}\right)_3 \\ \Delta \left(\frac{1}{n^2}\right)_4 \\ \Delta \left(\frac{1}{n^2}\right)_5 \\ \Delta \left(\frac{1}{n^2}\right)_6 \end{bmatrix} = \begin{bmatrix} r_{11} & r_{12} & r_{13} \\ r_{21} & r_{22} & r_{23} \\ r_{31} & r_{32} & r_{33} \\ r_{41} & r_{42} & r_{43} \\ r_{51} & r_{52} & r_{53} \\ r_{61} & r_{62} & r_{63} \end{bmatrix} \begin{bmatrix} E_1 \\ E_2 \\ E_3 \end{bmatrix} \quad (35)$$

The 6×3 matrix above is called the electrooptic tensor.

In general, the application of an electric field changes the principal axes. The new pricipal axes are found by diagonalizing the following matrix[41].

$$
\begin{bmatrix}
\Delta\left(\frac{1}{n^2}\right)_1 & \Delta\left(\frac{1}{n^2}\right)_6 & \Delta\left(\frac{1}{n^2}\right)_5 \\
\Delta\left(\frac{1}{n^2}\right)_6 & \Delta\left(\frac{1}{n^2}\right)_2 & \Delta\left(\frac{1}{n^2}\right)_4 \\
\Delta\left(\frac{1}{n^2}\right)_5 & \Delta\left(\frac{1}{n^2}\right)_4 & \Delta\left(\frac{1}{n^2}\right)_3
\end{bmatrix}
\tag{36}
$$

For SBN, the non-zero electrooptic tensor elements are $r_{13} = r_{23} = 47$ pm/V[39] , $r_{42} = r_{51} = 42$ pm/V[40], and $r_{33} = 235[39]$, 420[40] pm/V. If the write pulses are aligned such that the grating wavevector is pointing in the z-coordinate direction, the space-charge field points in that direction as well. In this case, for SBN, Eq. 35 becomes

$$
\begin{bmatrix}
\Delta\left(\frac{1}{n^2}\right)_1 \\
\Delta\left(\frac{1}{n^2}\right)_2 \\
\Delta\left(\frac{1}{n^2}\right)_3 \\
\Delta\left(\frac{1}{n^2}\right)_4 \\
\Delta\left(\frac{1}{n^2}\right)_5 \\
\Delta\left(\frac{1}{n^2}\right)_6
\end{bmatrix}
=
\begin{bmatrix}
0 & 0 & 47 \\
0 & 0 & 47 \\
0 & 0 & 235,420 \\
0 & 42 & 0 \\
42 & 0 & 0 \\
0 & 0 & 0
\end{bmatrix}
\begin{bmatrix}
0 \\
\cdot \\
0 \\
E(t)
\end{bmatrix}
.
\tag{37}
$$

It can be seen using Eq. 32 that no 'mixed' terms enter into the index ellipsoid equation because from Eq. 37, $\Delta\left(\frac{1}{n^2}\right)_{4,5,6} = 0$. This means that the principal dielectric axes are not changed. This can be seen because the matrix Eq. 36 is already diagonal for the above case. From the magnitudes of the tensor elements for SBN it is obvious that the greatest change in index will be that for the z-direction, $\Delta\left(\frac{1}{n^2}\right)_3$. In the experimental section this fact will be cited as the reason for the probe beam having its polarization in the z-direction. Using the solution to Eq. 27 for the space-charge field in Eq. 37 yields an equation for the time dependence of the change in index of refraction of the crystal.

Under illumination with two beams crossing, and hence interfering, in the sample there are bright and 'dark' spatial bands as described by the equation just prior to Eq. 15. If the grating wavevector is in the z- coordinate direction, the intensity vs. position plot is shown in Figure 2a. As was discussed above, the

charge carriers (assume electrons for now) are excited into the conduction band in the bright regions, drift and diffuse to the dark regions, and become trapped there. This results in a charge density distribution, ρ_{sc}, as shown is Figure 2b. In turn, this results in a space-charge field that is phase shifted from the intensity and charge distributions as is shown in Figure 2c. Through the electrooptic effect as discussed above this space-charge field modulates the index of refraction. This modulation is shown in Figure 2d.

During the build-up and decay of this index grating a laser beam is passed through the sample such that is satisfies the Bragg condition for maximum scattering from the grating. A brief description of optimum light diffraction by thick holograms is presented here. It will follow section 2.5 of reference [26]

For optimum light diffraction from thick holograms the grating wavevector, k_g, must be exactly equal to the incident and diffracted probe beam wavevectors. This is shown pictorially in Figure 3, where k_d is the diffracted wavevector and k_i is the incident wavevector. So, given an optical interference pattern that establishes an index grating wavevector, the angle at which the probe beam must be incident is determined from laws of conservation of energy and momentum. These arguments lead to the relations:

$$\omega_d = \omega_i \tag{38}$$

and

$$\mathbf{k}_d = \mathbf{k}_i \pm \mathbf{k}_g. \tag{39}$$

Eq. 39 leads us to the required conditions for the incident angle:

$$\theta_i = \sin^{-1}\left[\frac{\lambda}{2\Lambda}\right] \tag{40}$$

where θ_i is the angle of probe beam incidence and $\Lambda = \frac{\lambda}{2\sin\theta}$ is the grating spacing.

Two Photon Absorption

Two photon absorption was first explained theoretically by Maria Goppert-Mayer in 1931[31]. Its observation experimentally had to wait until the development of the laser. The first reported observation was made by Kaiser and Garrett
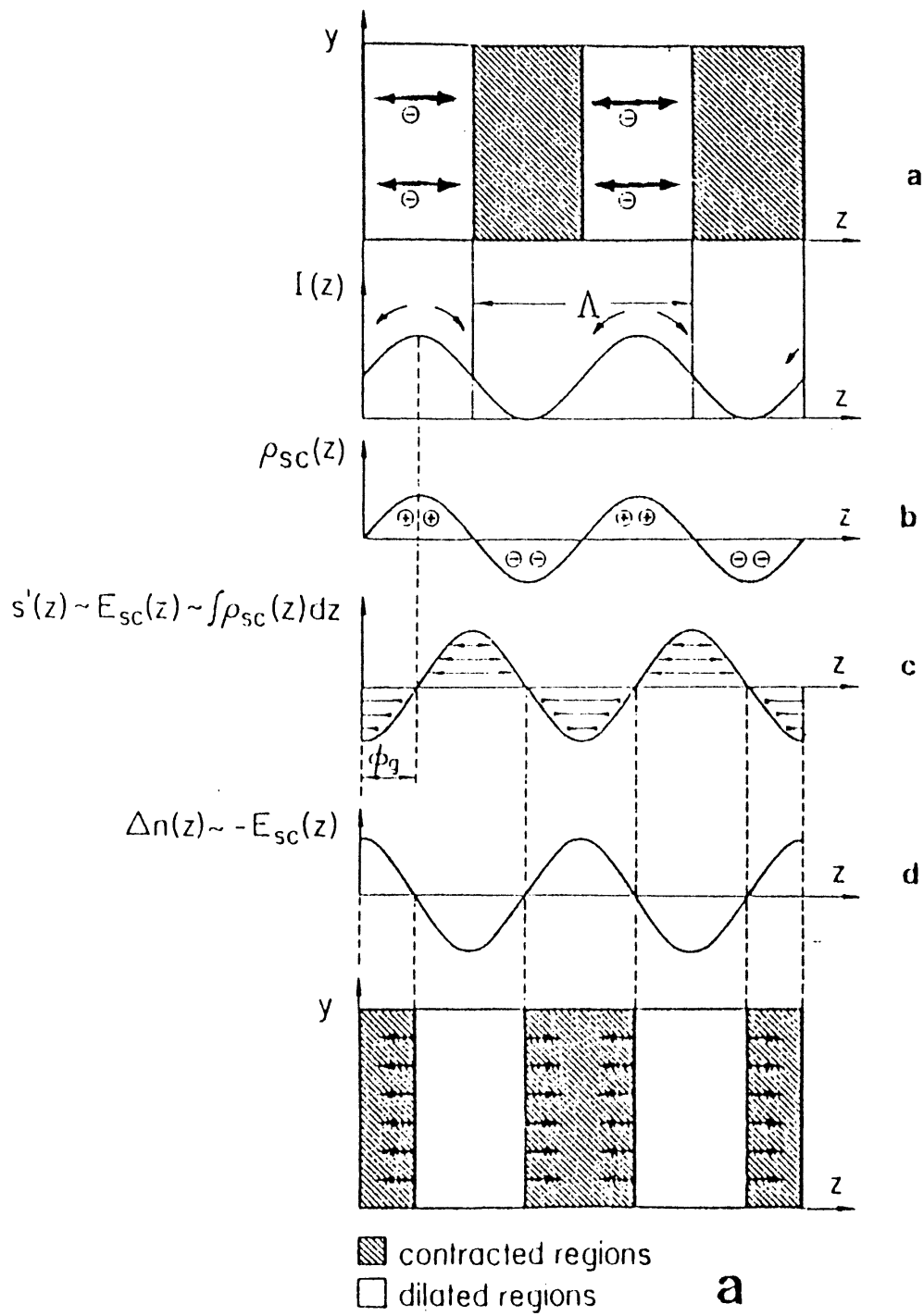
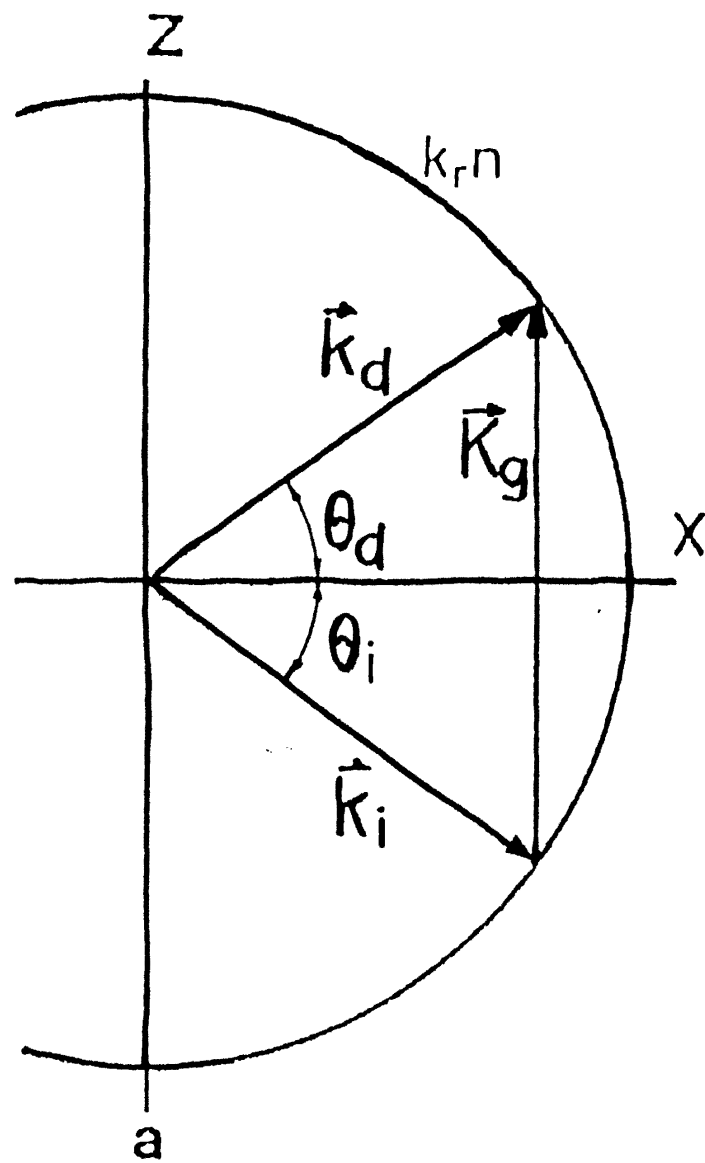Figure 2. Build-up of the space-charge field, E_{sc}. [25]

Figure 3. Wavevector diagram for isotropic Bragg diffraction. [25]

in 1961[32] who illuminated a crystal of Eu^{2+}:CaF_2 with a ruby laser beam. Upon excitation, the crystal emitted the characteristic fluorescence of an excited state of Eu^{2+} at 425nm. This blue fluorescence had been previously observed only under uv illumination. Since there is no measurable linear absorption at the ruby laser wavelength to allow for successive single photon absorption, apparently two photons were simultaneously absorbed to account for the high energy transition to the excited state. There have been several experimental techniques developed in order to study two photon absorption. One technique used is the measurement of the transmitted energy through a medium as a function of incident energy. A spectroscopic technique is used as well. It involves the measurement of the luminescence from a material that has been pumped by two photon absorption. A third technique is the measurement of the conductivity of a material after two photon absorption. The first experimental technique listed above is of interest. A theoretical model used in describing experimental results for this technique is presented here.

The differential equation describing the intensity (I) depletion of an electromagnetic plane wave after propagation of a length, z, in an isotropic material is given by[33]

$$\frac{dI}{dz} = -\alpha I - \beta I^2 \tag{41}$$

if only I and I^2 dependencies are assumed. In Eq. 41, α is the linear absorption coefficient and β is the two photon absorption coefficient. In general, β can have contributions from a number of physical processes other than the simultaneous absorption of two photons. Two of which are: 1) single photon absorption by the free carriers produced by the pulse and; 2) single photon absorption following second harmonic generation. Given certain experimental conditions each of these contributions can be negligible (see experimental section).

For beam propagation in the z-coordinate direction, the solution of Eq. 41 has the following form:

$$I(x,y,z) = \frac{I(x,y,0)e^{-\alpha z}}{1 + \frac{\beta}{\alpha}I(x,y,0)(1 - e^{-\alpha z})}. \tag{42}$$

A single reflection from the front and back surfaces is easily included to obtain

$$I(x,y,z) = \frac{(1-R)^2 I(x,y,0)e^{-\alpha z}}{1 + \frac{\beta}{\alpha}(1-R)I(x,y,0)(1 - e^{-\alpha z})}, \tag{43}$$

where R is the intensity reflection coefficient.

Since the experimentally measured quantity is the energy, it is necessary to determine the spatial and temporal profiles of the pulse. This allows for a conversion from energy to intensity. For the experiments presented below, the temporal profile is taken as a gaussian for all cases. However, two types of spatial profiles are used to model experimental conditions: 1) Gaussian and 2) uniform.

In the case that the spatial and temporal profiles are both gaussian, the transmitted intensity can be written[34]

$$I(x,y,z,t) = \frac{(1-R)^2 I_0 e^{-(t/\tau)^2} e^{-(r/r_0)^2} e^{-\alpha z}}{1 + \frac{\beta}{\alpha} I_0 e^{-(t/\tau)^2} e^{-(r/r_0)^2}(1-R)(1 - e^{-\alpha z})}. \tag{44}$$

Where I_0 is the maximum intensity of the pulse, $I_0 = \frac{E_0}{(\pi r_0^2)\sqrt{\pi}\tau}$, r_0 is the radius at the e^{-1} point, and τ is the half width at the e^{-1} point.

The energy transmission coefficient through a sample of length l is then given by[34]

$$T = \frac{\iiint I(x,y,l,t)dxdydt}{\iiint I(x,y,0,t)dxdydt} = \tag{45}$$

$$\frac{2\alpha e^{-\alpha l}(1-R)}{\beta I_0 \sqrt{\pi}(1-e^{-\alpha l})} \int_0^\infty \ln\left[1 + \frac{\beta}{\alpha} I_0(1-R)(1 - e^{-\alpha l})e^{-x^2}\right] dx$$

This expression represents the basic equation used to arrive at a value for β from the experimental measurements of T vs. I_0 for the case of gaussian profiles.

Taking the spatial profile to be uniform and the temporal profile to be gaussian, Eq. 44 becomes

$$I(x,y,z,t) = \frac{(1-R)^2 I_0 e^{-(t/\tau)^2} e^{-\alpha z}}{1 + \frac{\beta}{\alpha} I_0 e^{-(t/\tau)^2}(1-R)(1 - e^{-\alpha z})} \tag{46}$$

where I_0 retains its definition from above.

The energy transmission coefficient, in this case, through a sample of length l is then given by[38]

$$T = \frac{(1-R)^2 e^{-\alpha l}}{\sqrt{\pi}\tau} \int_{-\infty}^\infty \frac{dt}{e^{(t/\tau)^2} + \frac{\beta}{\alpha} I_0(1-R)(1 - e^{-\alpha l})}. \tag{47}$$

In order to fit data using Eq.'s 45 and 47 the integration contained in the the expression for T must be done numerically.

CHAPTER III

EXPERIMENTAL

In the experiments reported here two different laser systems were used: 1) picosecond and; 2) subpicosecond. The picosecond laser source was the frequency doubled output of a Continuum model YG571C Q-switched and mode locked Nd:YAG laser operating at 10 Hz (λ = 532 nm). Each pulse had a duration, full width at half maximum (FWHM), of 20 picoseconds with a typical energy at the sample of 1 mJ. This energy could be varied using a polarizing beam splitter preceded by a polarization rotator. The subpicosecond laser source used was the amplified output of a Spectra-Physics model 3500 synchronously pumped femtosecond dye laser. An intracavity birefringent tuner was used to select a wavelength of 580 nm which corresponds to the peak of the Rhodamine 6G dye lasing curve. The 350-450 fsec duration dye laser pulses (82 MHz) were then amplified by a three stage pulsed dye amplifier (PDA). The dye used in all three stages was Kiton Red. The PDA was pumped by a Spectra-Physics model GCR-3 injection seeded, Q-switched Nd:YAG laser. This laser was synchronized with the pump source of the dye laser such that it amplified one of the pulses in the 82 MHz pulse train every 33.3 ms producing a 30 HZ output of high energy pulses. Energies at the sample were typically 1 μJ. The pump source for the dye laser was a Spectra-Physics model 3800 cw, mode locked Nd:YAG laser whose pulses were compressed via the standard optical fiber/grating pair method and then frequency doubled.

The gratings written in SBN:60 and Fe:SBN:60 with a single laser pulse last longer than the time between pulses for both laser systems. For this reason a single pulse needed to be extracted from each pulse train in order to do the experiments. Single subpicosecond pulses were obtained by manual operation of the Q-switch of

21

the Nd:YAG laser used to pump the PDA. For the picosecond laser a mechanical shutter was used.

Two Photon Absorption

An important mechanism for the production of free carriers in insulating crystals when using high intensity, visible light laser pulses is two photon absorption (TPA). In order to obtain an idea of the contribution in SBN:60 and Fe:SBN:60, the TPA coefficient was measured using both lasers. It should be noted from the start that certain precautions, such as continuous monitoring the spatial and temporal profiles of the pulses during the experiment, were not taken. The effect of random variations in pulse length and spatial profile is a less accurate value for β than what could be obtained under ideal conditions. Bechtel *et. al.*[34] discuss spatial and temporal fluctuations in laser pulses during TPA coefficient measurements and state that they result in overestimations.

The experimental setup used to measure the energy transmission coefficient as a function of incident pulse energy is shown in Figure 4. The incident energy was varied using a polarizing beam splitter preceded by a polarization rotator. Since the measurement of the TPA coefficient was performed to estimate its contribution to free carrier production in the photorefractive experiments, the polarization of the pulses was maintained such that it was the same as a write pulse in those experiments: perpendicular to the plane of incidence. The incident and transmitted laser pulse energies were measured with a Laser Precision model RM-6600 universal radiometer with two model RJP-735 probes.

The spatial profile of the picosecond pulses was obtained by scanning a 15 micron pinhole across the pulse path while monitoring the amount of transmitted light with a photodiode. The data obtained for the picosecond source is shown in Figure 5. A gaussian fit was performed yielding a e^{-1} radius of $r_0 = 0.061$ cm. The spatial profile of the subpicosecond source is shown in Figure 6. The shape is best modeled by a uniform spatial profile with a radius of 0.8 cm. The temporal profile of both laser systems was taken to by gaussian with half-widths at the e^{-1}
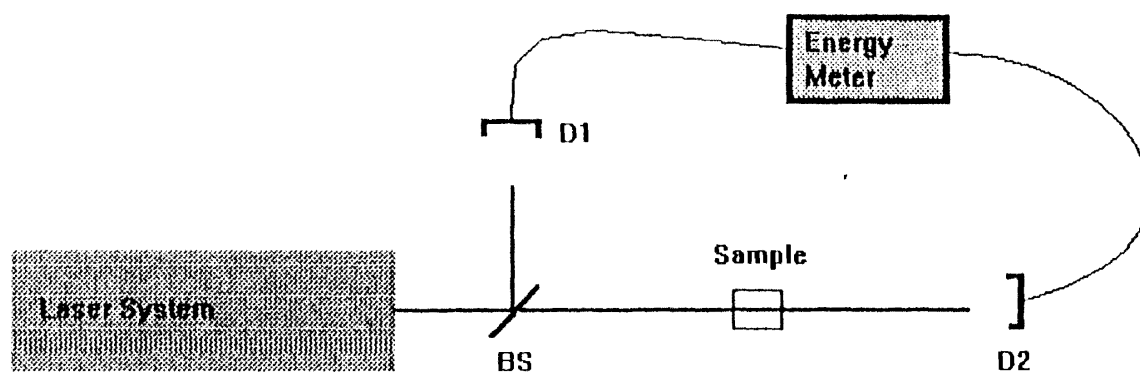
Figure 4. Experimental setup for two photon absorption measurements.

point of $\tau_{ps} = 13$ ps and $\tau_{fs} = 240$ fs for the picosecond and subpicosecond lasers respectively.

In Eq.'s 45 and 47 the value of intensity reflection coefficient is needed to calculate the energy transmission coefficient. The value was calculated using the equation[43]

$$R = \left| \frac{n\cos(i) - \sqrt{n_0^2 - n^2\sin^2(i)}}{n\cos(i) + \sqrt{n_0^2 - n^2\sin^2(i)}} \right|^2 \tag{48}$$

where n is the index of refraction of air, n≈ 1, and n_0 is the index of refraction of the crystal, and i is the angle of incidence. Using the published value for $n_0 = 2.33[1]$, and the angle of incidence, i=3.2°, R=0.16. The value for the index of refraction was confirmed to be valid for our particular samples by a simple Brewsters angle experiment and calculation.

As was mentioned in the theoretical chapter, the value for β in Eq. 41 can have contributions from physical processes other than the simultaneous absorption of two photons. Single photon absorption by free carriers produced by the pulse can lend an important contribution under certain conditions. In order to eliminate the possibility of significant contribution from this effect an experiment was set up so that a weak probe pulse passed through the sample 2 ps behind a strong pump pulse. The probe was a split component of the strong pulse and 1000 times less intense. A mechanical delay line was used to obtain the 2 ps time difference. If there were free carrier absorption the probe pulse would have been attenuated increasingly as the strong pulse energy was increased. Transmitted probe pulse energies were recorded as a function of incident strong pulse energies. The transmitted probe pulse energies were also recorded in a separate instance when the strong pulse was blocked from entering the sample. This was used to check the effects of the strong pulse on the probe. Except for a small increase in the transmission of the probe pulse at lower energies its transmission was unaffected by the presence of the strong pulse. This is seen in Figure 7. This result supports, to a good approximation, the exclusion of single photon free carrier absorption in the calculation of β. The increased transmission of the probe pulse for low pump
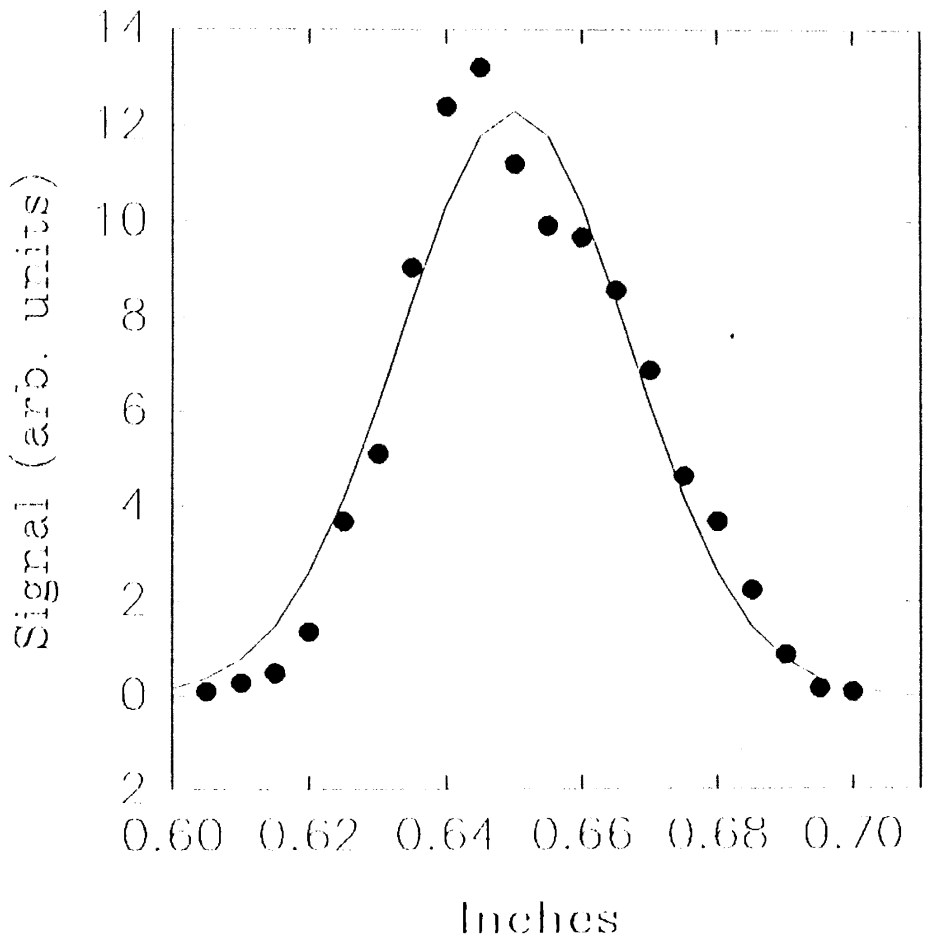
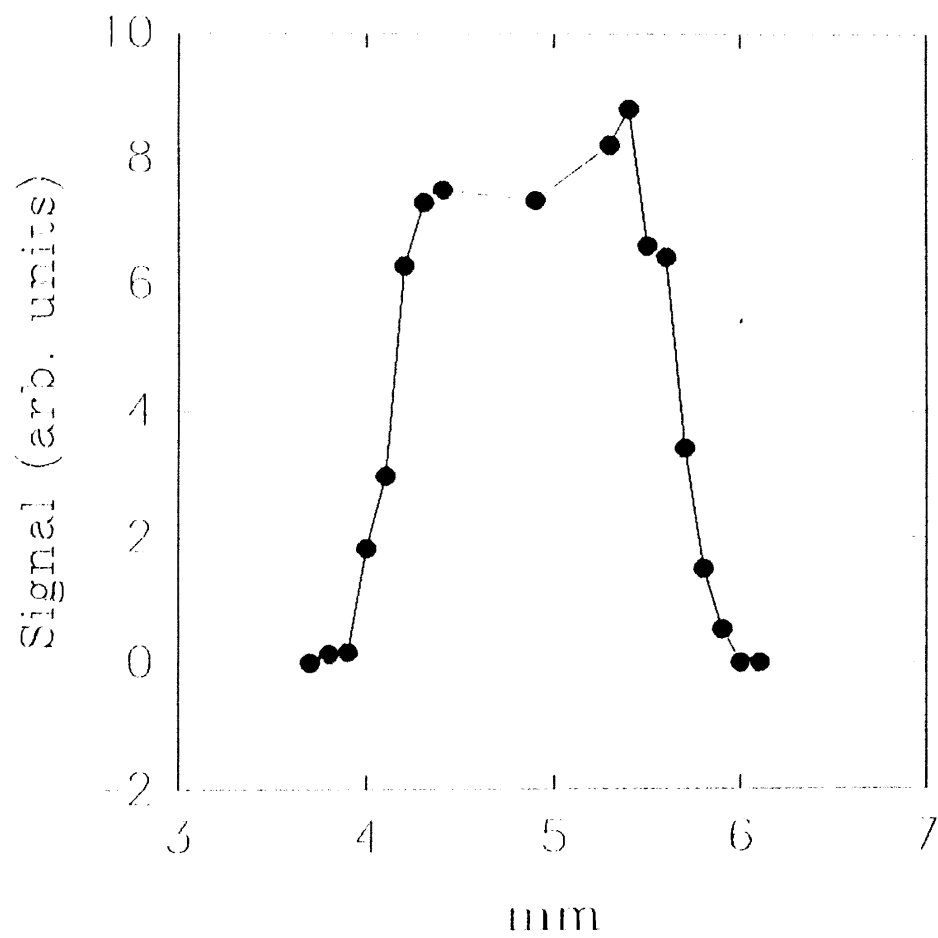Figure 5. Spatial profile of picosecond laser system pulses.

Figure 6. Spatial profile of subpicosecond laser system pulses.

pulse energies could by due to an initial saturation of the linear absorption that is compensated for by another process at higher energies.

Single photon absorption following second harmonic generation also lends a contribution to the β in Eq. 41 because the second harmonic of 532 nm or 580 nm lies well within the intrinsic absorption range of SBN:60 and Fe:SBN:60. This effect is thought to be negligible in this case because second harmonic generation relies heavily on the phase matching condition which is not satisfied in the experiments reported here.

The energy transmission coefficient was measured for both samples by passing a single 20 ps pulse (λ = 532 nm) through each while monitoring both the transmitted and incident energies. The resulting data is plotted in Figure 8 where the abscissa is the ratio, T, of transmitted to incident intensities. The following program was written in order to fit Eq. 45 to this data.

$$p = Table[i, \{i, 7 \ 10^{\wedge} - 7, 3.5 \ 10^{\wedge} - 5, 2.275 \ 10^{\wedge} - 6\}];$$

$$a = 0.045$$

$$ss = 0.012$$

$$tau = 13.2 \ 10^{\wedge} - 12$$

$$beta = 2.3 \ 10^{\wedge} - 9$$

$$b = (.95 \ (ss) \ Sqrt[Pi] \ tau/(beta \ p)) \ ((a \ Exp[-a \ 0.5])) \times$$

$$Log[1 + 0.84 \ beta \ p \ (1/(Sqrt[Pi] \ tau \ ss)) \ Exp[-x^{\wedge}2] \ ((1 - Exp[-a \ 0.5])/a)];$$

$$c = Table[NIntegrate[Part[b, i], \{x, o, Infinity\}], \{i, 1, 15\}];$$

$$d = Table[\{Part[Part[p, i], Part[c, i]\}, \{i, 1, 15\}];$$

$$z = ListPlot[d, PlotJoined-> True, Axes-> False];$$

$$e = ReadList["b: /sbnbeta.prn", \{Number, Number\}];$$

$$y = ListPlot[e, PlotStyle-> PointSize[1/100], Axes-> False];$$

$$Show[y, z].$$

$$(49)$$

p corresponds to the energy range of incident pulses, a is the length of the crystal, ss is the cross sectional area of the pulse, tau is the half-width at the e^{-1} point, and
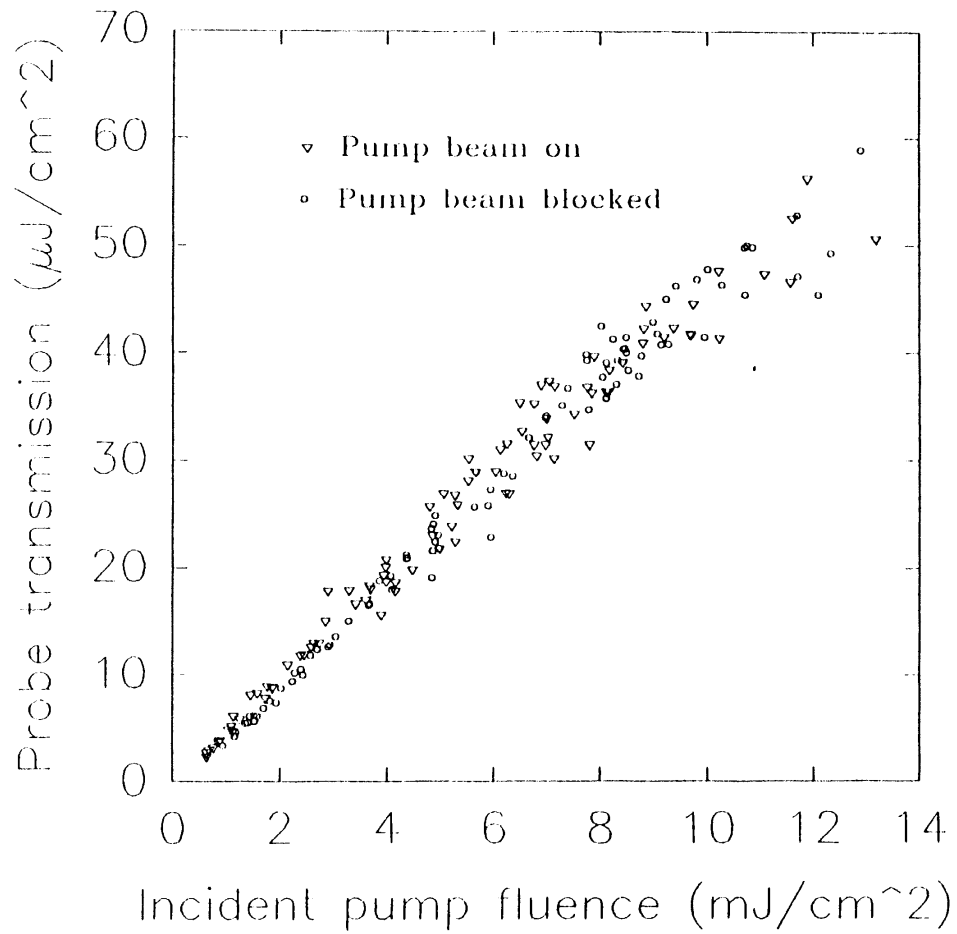
Figure 7. Results of the experiment to eliminate from the TPA coefficient single
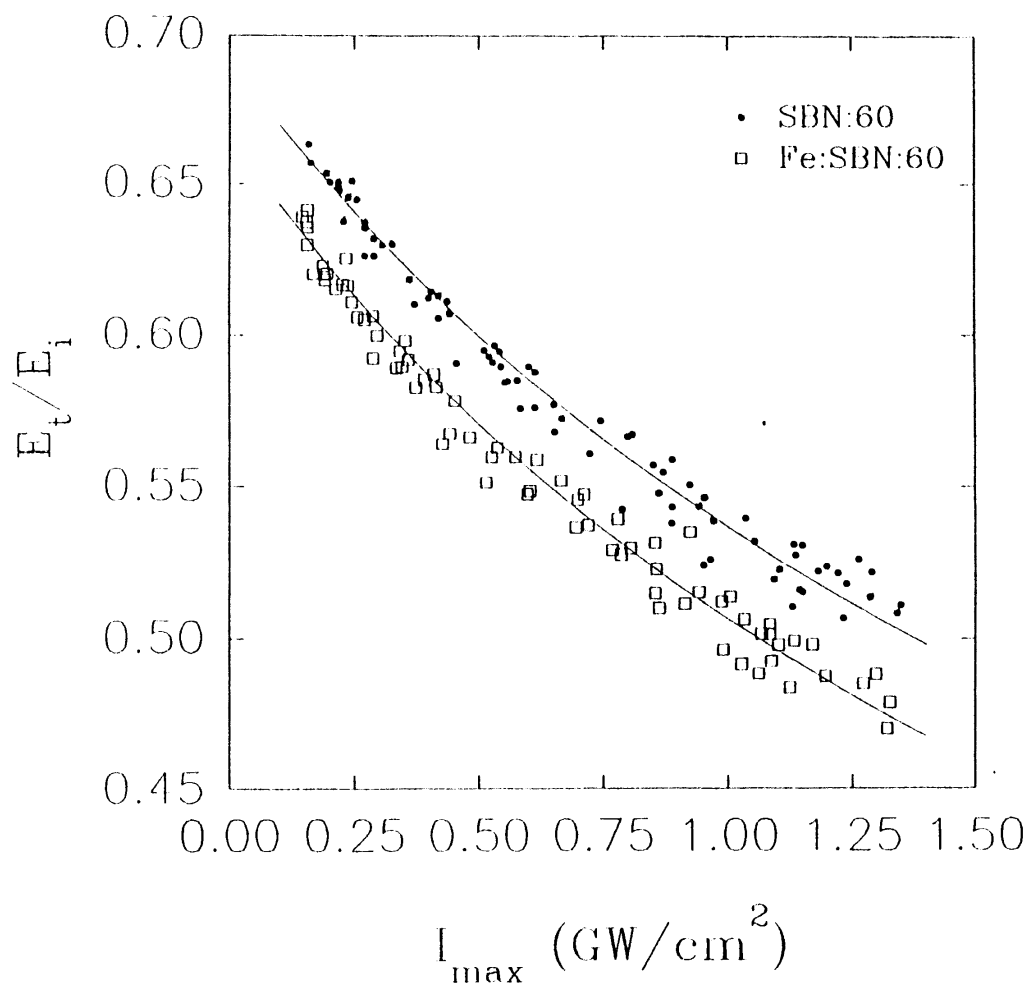photon absorption by free carriers.

Figure 8. Data and theory graphs for TPA in SBN:60 and Fe:SBN:60 using the picosecond laser system (532 nm).

beta is the two photon absorption coefficient. This program runs in the commercial software package Mathematica in order to do the numerical integration. Both α and β were allowed to vary as free parameters. The solid lines in the figure represent the results of the fitting procedure. The parameters for the undoped sample were, $\alpha = 0.05$ cm^{-1} and $\beta = 2.25 - 2.35$ cm/GW, and for the Fe-doped sample were, $\alpha = 0.1$ cm^{-1} and $\beta = 2.1 - 2.2$ cm/GW.

The same experiment was performed on the undoped sample using the sub-picosecond laser system operating at a wavelength of 580 nm. The resulting data is plotted in Figure 9. As can be seen this data contains more scatter in comparison with the data when using the picosecond laser system. This could possible be due to the fluctuation of pulse length and spatial profile during the experiment that is inherent when using this type of subpicosecond laser system. A modification of the above program was used in order to fit Eq. 47 to the subpicosecond data. The parameters ss, tau, p, and beta were changed to coincide with experimental conditions for the subpicosecond laser system and Eq. 47 was used for b instead of Eq. 45. A reasonable fit to the data could only be arrived at by incorporating a linear background of approximately 18% into the theory. Although this erases the physical validity of the parameters in the equation that determine the vertical position of the graph, it should yield an appropriate approximation for the parameter that determines the curvature, β. The resulting value for the TPA coefficient was 2 cm/GW in reasonable agreement with the TPA coefficient measured at the shorter wavelength of 532 nm.

Four Wave Mixing

Single laser pulses were used to induce refractive index gratings in nominally undoped and iron-doped SBN:60 using both 20 ps ($\lambda = 532$ nm) and 400 fs ($\lambda = 580$ nm) pulses. The experimental setup used is shown in Figure 10. A single laser pulse was split into two parts of equal energy (hereafter referred to as 'write' pulses) which were focused such that they overlapped spatially and temporally in the sample ideally producing a spatially harmonic interference pattern as
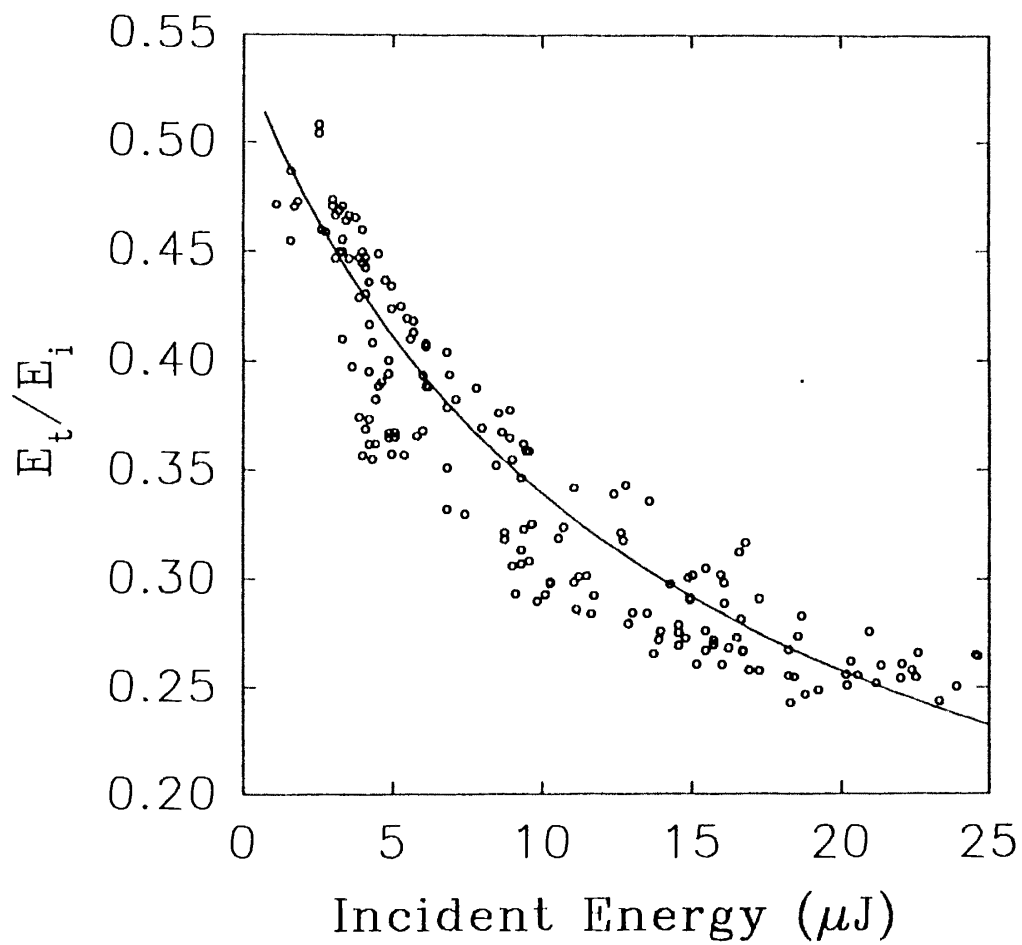
Figure 9. Data and theory graph for TPA in SBN:60 using the subpicosecond laser system (580 nm).

described by Eq. 14. The angle between the paths of the pulses was 3.2° measured in air. In order to monitor the build-up and decay of gratings formed by the write pulses, a low power, cw He-Ne laser laser aligned at the Bragg angle for optimum diffraction was also focused in the sample. The beam geometry and crystal orientation was the usual photorefractive configuration used to study SBN[42], i.e. the π-polarized He-Ne laser beam was crossed in the sample with the two σ-polarized write beams which were oriented such that they produced a grating wavevector that was parallel to the c-axis. As was discussed in the theoretical chapter, the probe beam polarization was chosen as above in order to realize the strongest electrooptic effects. For this geometry, the $r_{33} = 235, 420$ pm/V electrooptic tensor element is used to calculate the index change that the probe 'sees'. If the probe beams polarization would have been chosen as vertical the $r_{13} = 47$ pm/V would have been used which would have resulted in a lower diffraction efficiency. The index change is approximately proportional to the electrooptic tensor element. To improve the signal-to-noise ratio the probe beam propagation direction was aligned out of the plane containing the write pulses. The diffracted beam was detected using a photomultiplier tube with a rise time of approximately 2 ns and a digital storage oscilloscope. An interference filter at the He-Ne laser wavelength was used to ensure that no stray light from the pulsed laser entered the photomultiplier tube.

Results

Picosecond-pulse excitation. With excitation pulses of 20 ps duration and 532 nm wavelength there were two distinct temporal features seen in the FWM signal from both samples. Typical data obtained for the undoped sample are shown in Figures 11 and 12. After the initial unresolved build-up the first decay of the FWM signal is in the 100 ms time scale (Figure 11). This was followed by a comparatively slow rise that reaches its maximum after a few minutes. The start of this rise can be seen in Figure 12. In the case of a total write beam energy of 78
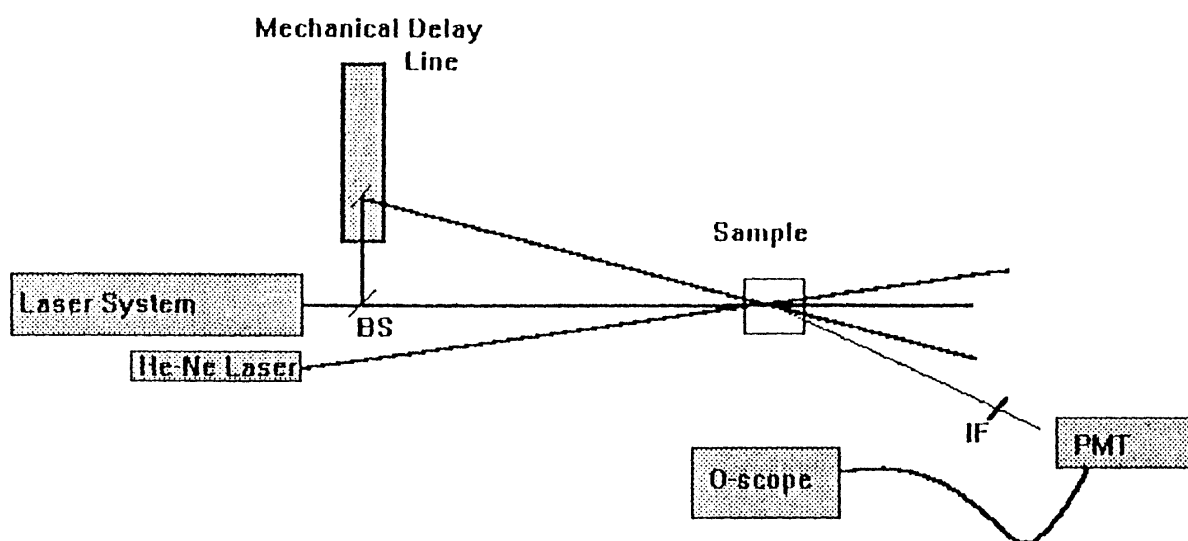
Figure 10. Experimental setup for FWM experiments.

μJ the second rise is complete in approximately four minutes and decays to half the peak height after another fifteen minutes.

Typical FWM data obtained using the Fe:SBN sample are shown in Figure 13-15. Similar to the signal from the undoped sample, there exists two stages to the signal in the time frame studied, however the time scales associated with them are very different. The decay of the first signal is complete in less than 25 ms and is followed by a rise of the second signal that is compete in less than 20 seconds. For pulse energies lower than those shown in Figures 13 and 14, e.g. Figure 15, the detected signal is observed to drop below the background level in the time regime just after the first signal decay. This means that there must be a process that has decreased the total amount of background light that is randomly scattered from the sample to the detector.

For both samples the cross-sectional are of interaction for the two write pulses was 2.7×10^{-5} cm^2.

Subpicosecond-pulse excitation. In a manner similar to what was seen using the picosecond pulses, excitation using 400 fs, 580 nm pulses produces two temporal features in the FWM diffracted signal in the time scale of interest in these experiments. Typical data are shown in Figures 16 and 17. The first feature in Figure 16 is a peak that has a rise time of 300-600 ns which is time resolved in Figure 17. This signal decays into the microsecond time scale where it competes with the rise of the second signal. The initial spike in the data seen in Figure 17 is due to gratings formed on the time scale of the temporal overlap of the two write pulses and was not of interest for this work. The time scales associated with the second peak depend upon the intensity of the write pulses. It has been observed to last as long as thirty seconds or as short as a few hundred milliseconds. It also should be noted that in the experiments using the subpicosecond laser source the resulting gratings written depended very strongly on the spatial overlap of the
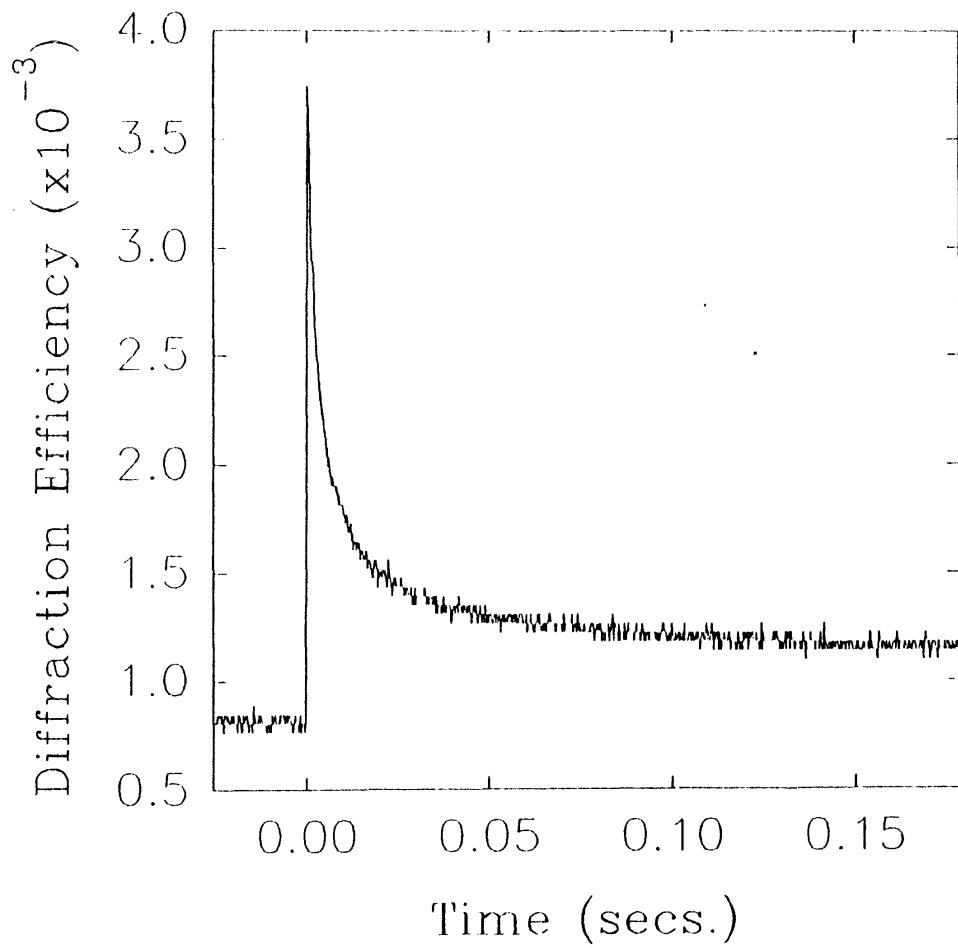
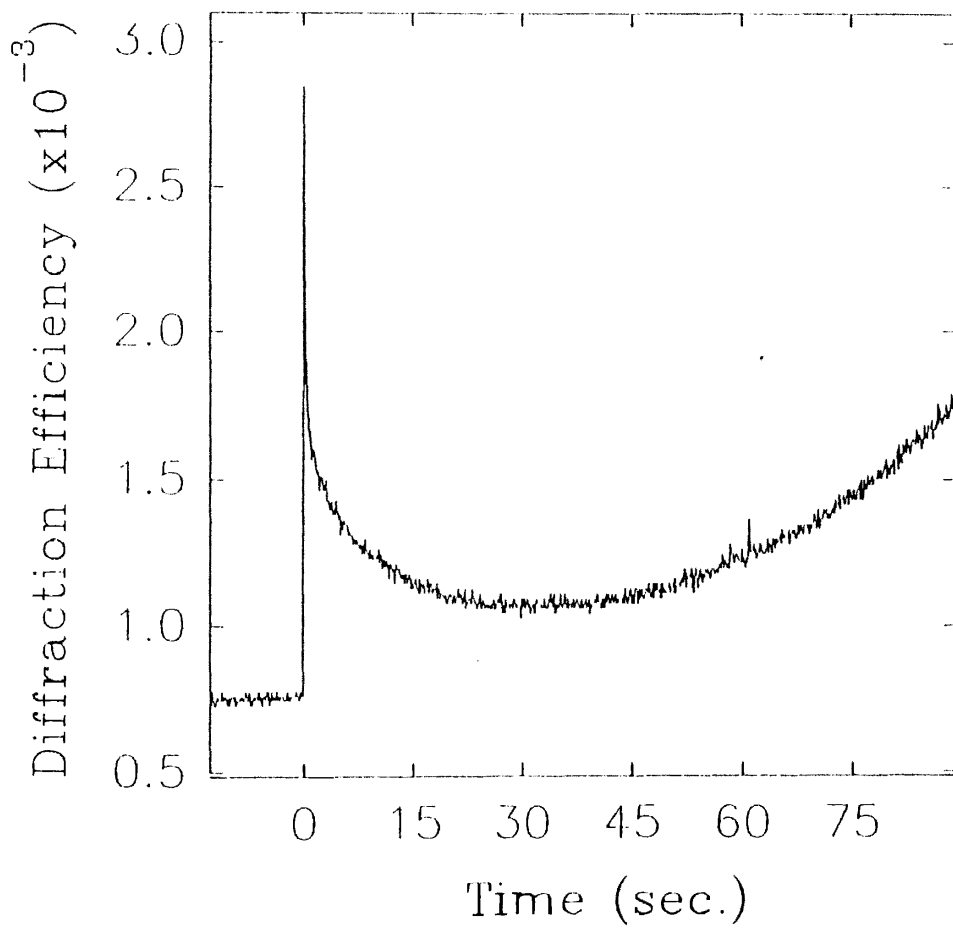Figure 11. FWM signal in SBN:60 following 47 microJoule, picosecond excitation.

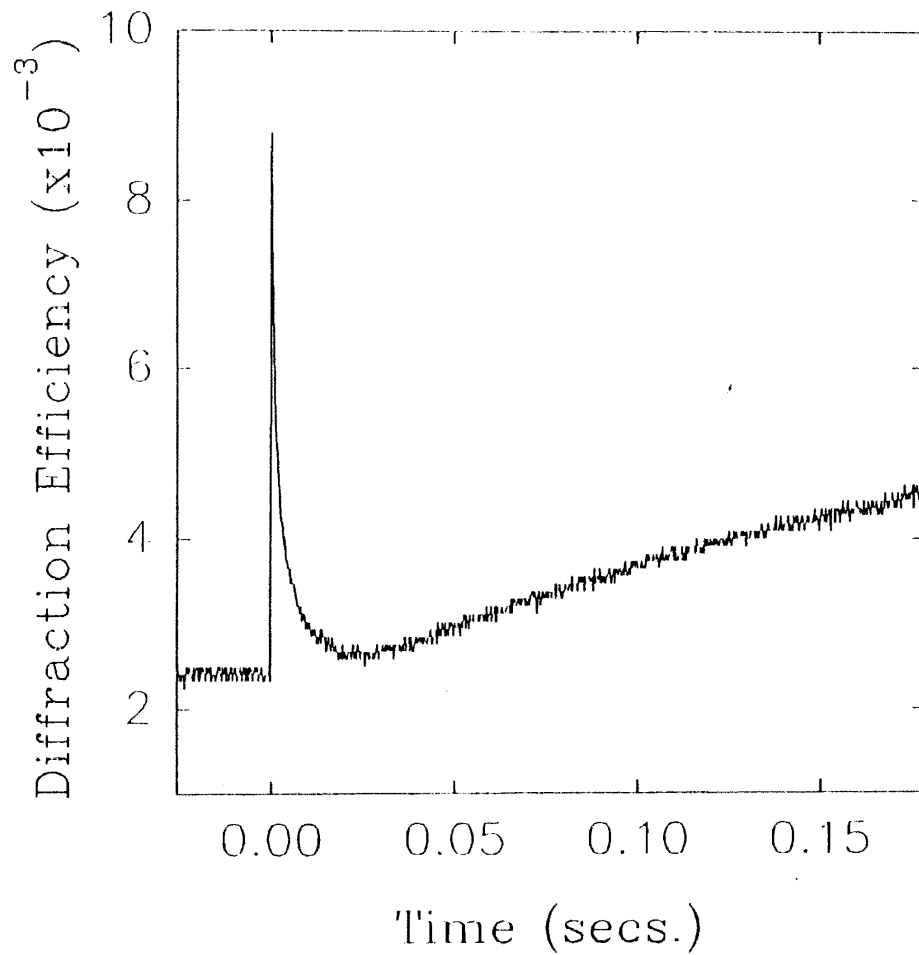Figure 12. FWM signal in SBN:60 following 46.4 microJoule, picosecond excitation.

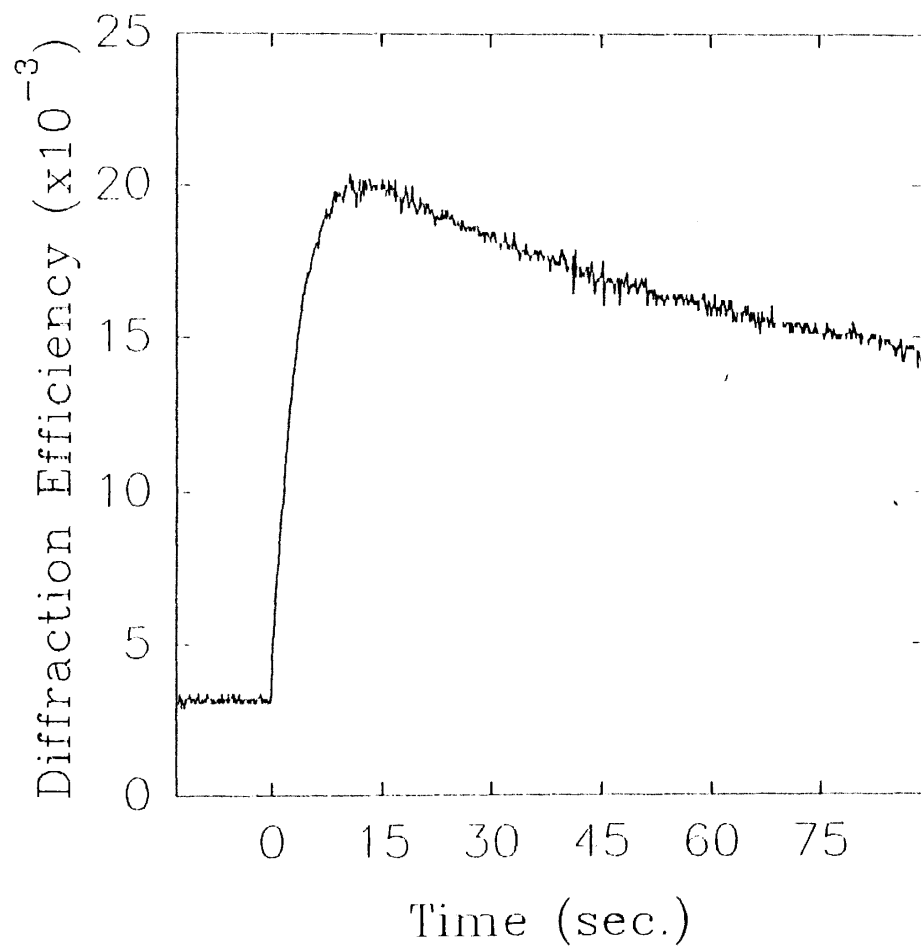Figure 13. FWM signal in Fe:SBN:60 following 42.8 microJoule, picosecond excitation.

Figure 14. FWM signal in Fe:SBN:60 following 50.0 microJoule, picosecond excitation.
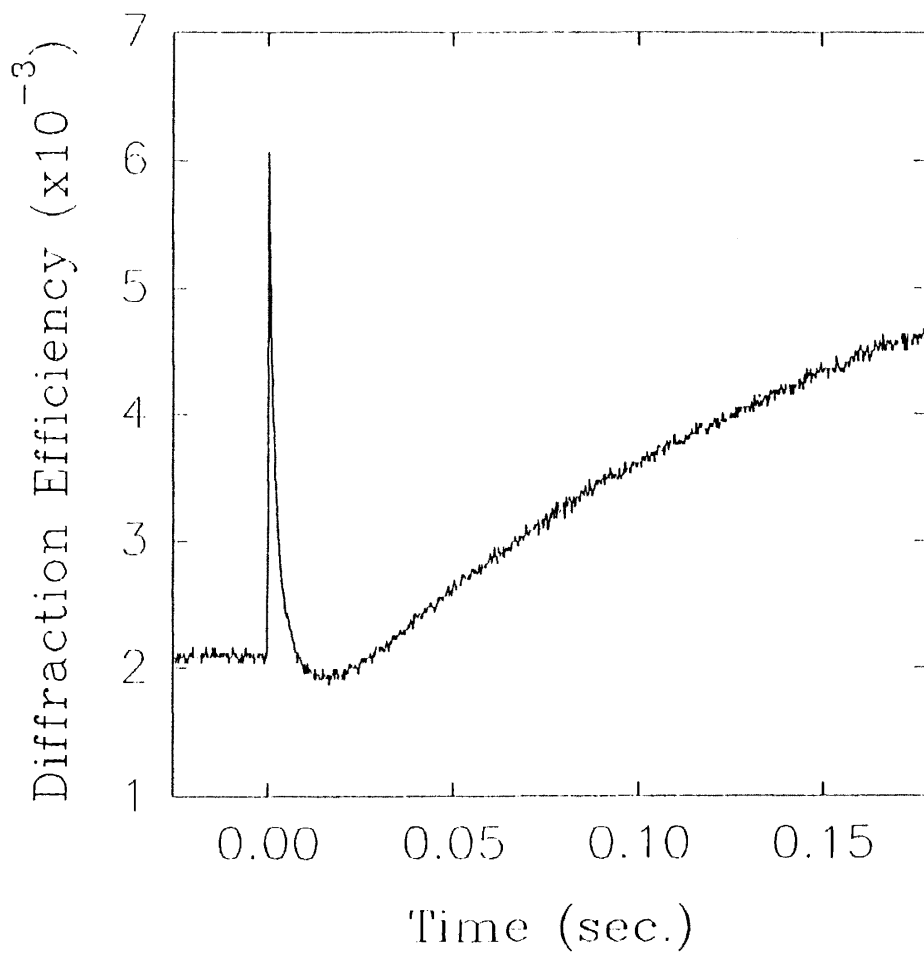
Figure 15. FWM signal in Fe:SBN:60 following 18.5 microJoule, picosecond excitation.

pulses. Very much care had to be taken to ensure repeatability. A strong dependence on spatial overlap was not observed using the picosecond source most likely because the spatial profile is much smoother and consistent.

Experiments on the Fe-doped samples were not performed using the subpicosecond laser system.

Discussion

Undoped sample. The first signal in the experiments using both the picosecond and subpicosecond laser systems is associated with scattering from a grating that is set up by an optically induced absorption change in the bright regions of the interference pattern of the two write pulses. A spatially harmonic absorption pattern is related to a spatially harmonic index of refraction change through the Kramers-Kronig relation. As an example consider a two level system where a change in absorption can be calculated from the absorption cross sections, σ_1 and σ_2, of the ground and excited states. The absorption coefficient K is given by the population density N_0 and N_1 of the two states

$$K = \sigma_0 N_0 + \sigma_1 N_1. \tag{50}$$

Changing the relative populations of the levels by optical excitation leads to a change in the absorption coefficient given by

$$\Delta K = -(\sigma_0 - \sigma_1)\Delta N, \tag{51}$$

where ΔN is the relative change in population. The Kramers-Kronig relation can be used to estimate the resulting change in index.

$$\Delta n = \frac{1}{2\pi^2} \int_0^\infty \frac{\Delta K(\lambda) d\lambda'}{1 - (\lambda'/\lambda)^2} \tag{52}$$

This equation is valid only for small changes in the absorption cross section. The preceding discussion was taken from reference [35].

In order to demonstrate that intense light at both 580 nm and 532 nm induces absorption at 632.8 nm, one of the write pulses and the He-Ne laser beam
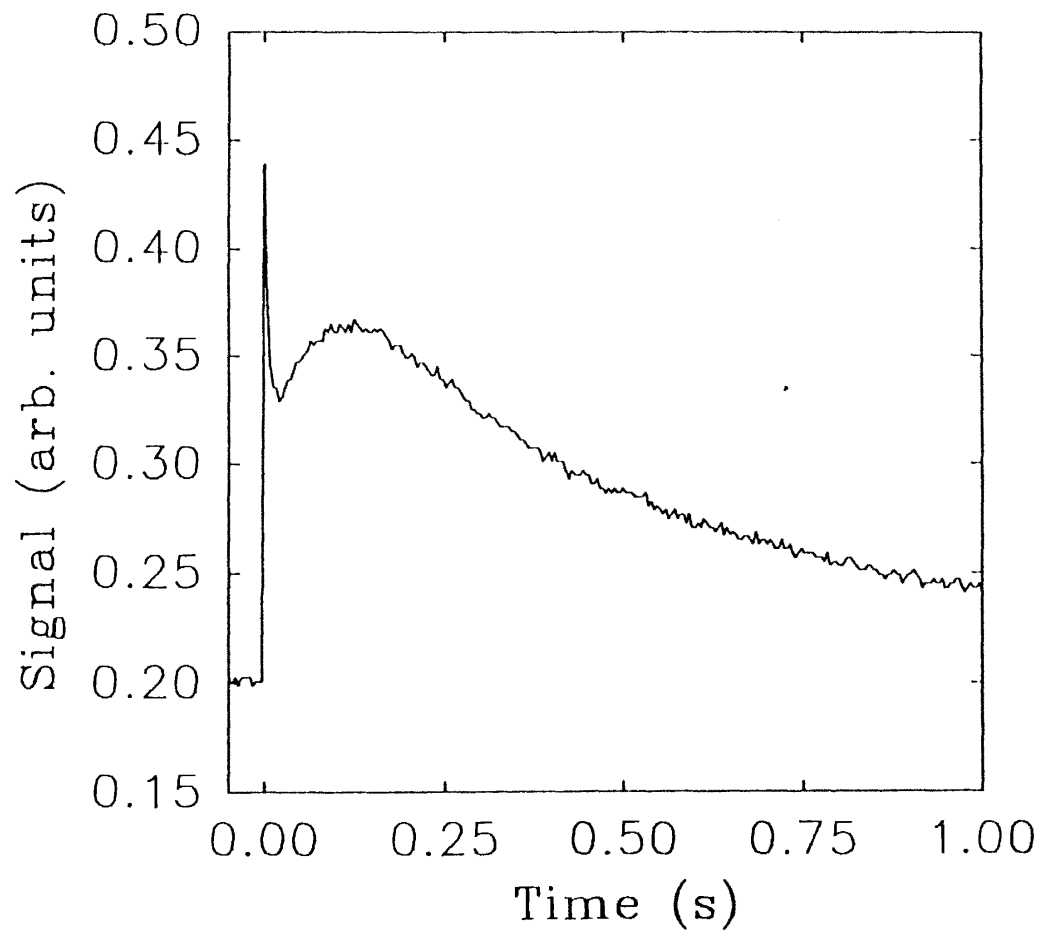
Figure 16. FWM signal in SBN:60 following 0.820 microJoule, subpicosecond excitation.
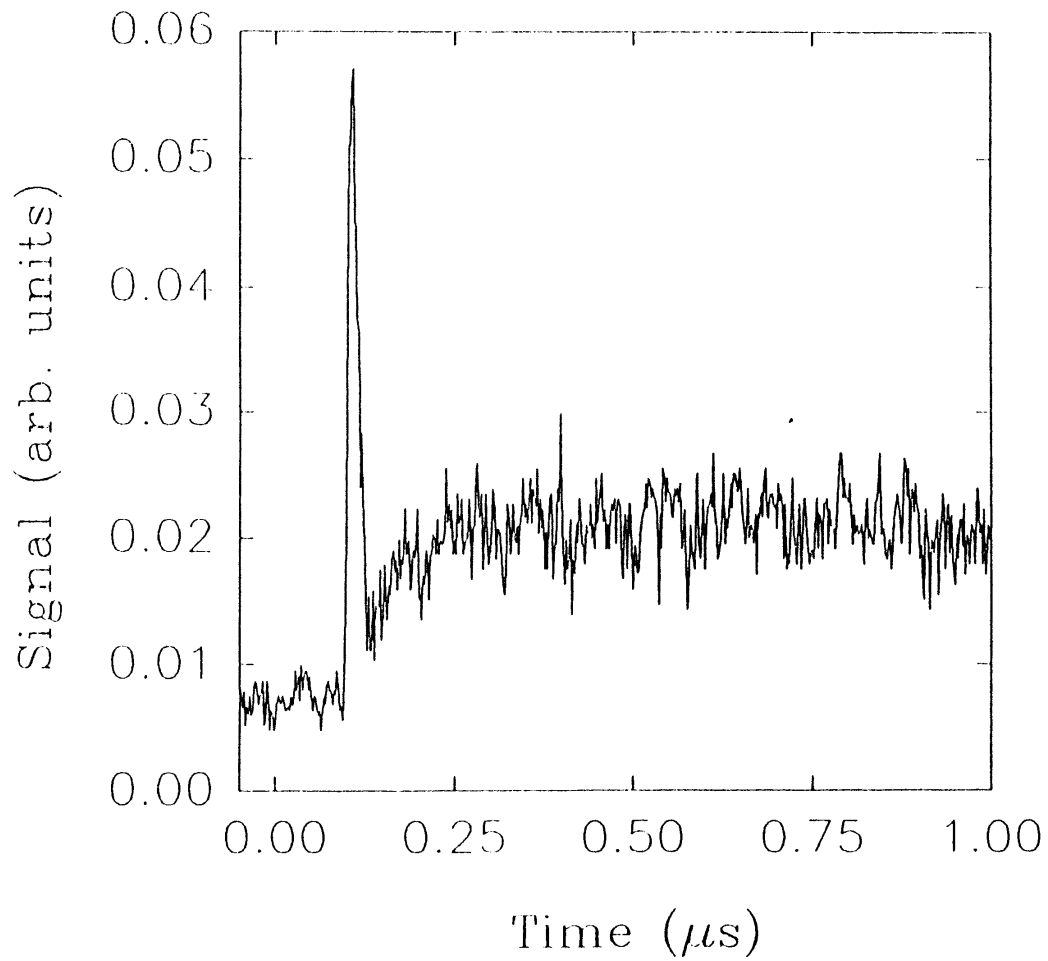
Figure 17. FWM signal in SBN:60 following 0.286 microJoule, subpicosecond
excitation.

were crossed in the sample and the transmitted He-Ne Laser was monitored with the same detection scheme as discussed above for FWM. The results of the experiment using the picosecond and subpicosecond laser systems are shown in Figure 18. In both cases, the time dynamics of the induced absorption are the same as those of the first peak of interest in the FWM experiments. It is interesting to note that the same type of probe beam depletion was observed using the green line (543nm) of the He-Ne laser as a probe. The recovery of the transmission, however, was noticeably slower for the shorter wavelength. This suggests that the site(s) responsible for the 543 nm absorption have a longer lifetime than those responsible for absorption at 632.8 nm. With the experiments described thus far it is not possible to determine the physical mechanisms responsible for the induced absorption. It is proposed that the induced absorption is a result of the population of an impurity or defect site that did not have significant population before excitation. Further, it is thought that significant population of this level can only be realized with the aid of significant two photon band-to-band transitions followed by trapping at the site(s) that absorb near 632 nm. The TPA coefficient at 532 nm, as discussed above, is 2.25-2.35 cm/GW. With an intensity of 2.5 GW/cm^2 the intensity depletion of the probe beam through SBN:60 is more than an order of magnitude greater than that of the linear absorption. Below this value of intensity, where the two photon contributions are not as great the transient probe beam depletion becomes an unmeasurable effect with our detection system. After excitation the free carriers populate an absorbing level at a rate that is roughly inversely proportional to the rise time of the induced absorption. The decay of the grating is due to the depopulation of the absorbing level either through recombination or trapping at other sites that do not absorb at 632.8 nm.

The subsequent rise of the diffracted signal after the decay of the absorption grating is explained as due to the usual charge displacement photorefractive effect as discussed in the theoretical chapter. It can only be observed when the beam geometry is such that photorefractive effects are possible. At this time the mechanism of charge transport as well as the sign of the charge carrier is not apparent.
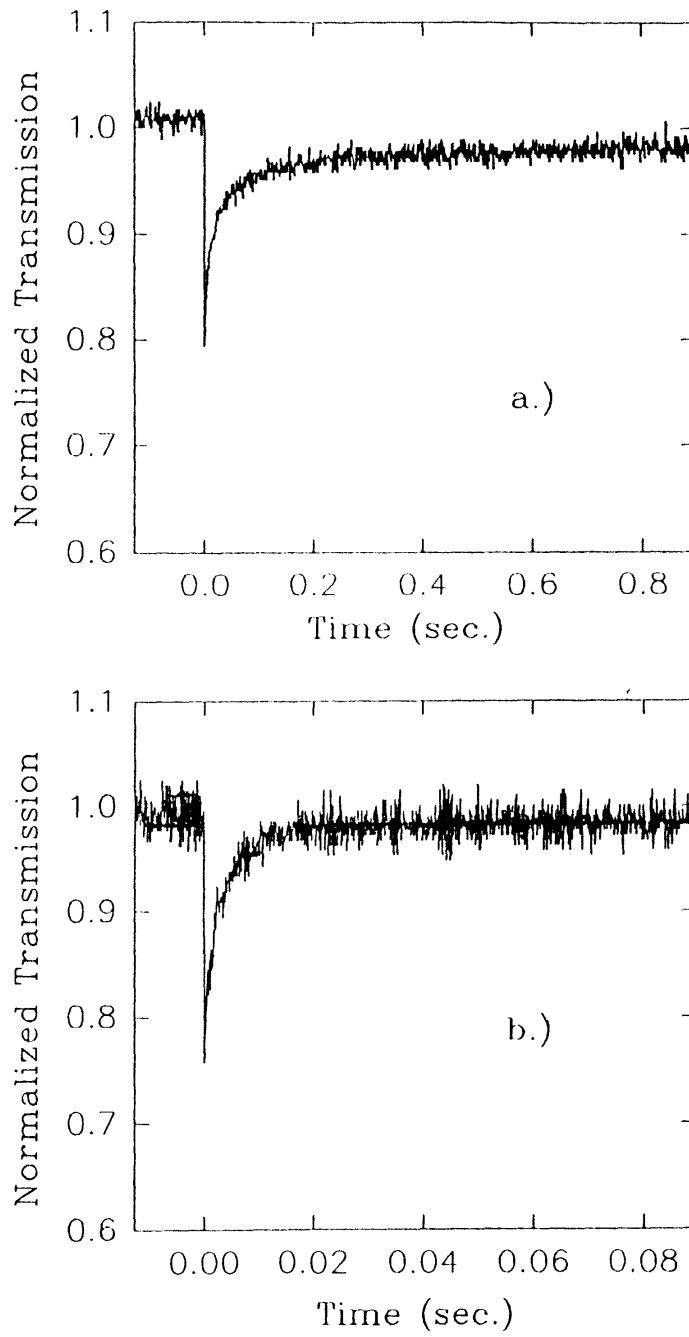
Figure 18. Probe beam depletion following a.) 46.1 microJoule, picosecond excitation and b.) 1.1 microJoule subpicosecond excitation.

In cw FWM experiments electrons have been found to be the dominant carrier[1]. However, competition from holes cannot be ignored in the pulsed regime because the direct band-to-band transitions that are associated with nonlinear absorption create a large number of holes. Their contribution to the grating depends on their relative mobility with respect to the electrons.

Fe-doped sample.   The time scales of the two temporal features of the FWM signal in Fe:SBN:60 are very different in comparison with the signal in the undoped sample. The first difference is seen in the much faster decay followed by a drop in the signal below the background level for the lower energies studied. This effect is not observed at higher intensities because the second rise begins at earlier times for increasing intensities and competes with the decay of the first signal. Such a drop in the signal below background can be explained by an increased absorption at the probe wavelength which, once the grating has decayed, reduces the amount of scattered light that passes through the sample to the detector. Since, in our model, the first signal is associated with induced absorption, the faster decay of the first signal would suggest that the induced absorption would also decay faster. On the contrary, however, the induced absorption experiment in the Fe-doped sample showed that the depletion lasted longer. This can be seen in Figure 19. This result indicates that the absorption grating is destroyed prior to the depopulation of the levels responsible for it. This suggests that the absorbing levels in the dark regions of the sample are populated on the time scale associated with the decay. Population of these levels reduces the contrast ratio of the grating and therefore the diffracted signal. Induced absorption is still present after the decay of the grating is complete which reduces the background scatter to the detector. This effect is not observed in the undoped sample because it does not have the advantage of increased carrier mobility due to the iron dopants. This increased mobility as a result of iron doping is also responsible for the faster build-up of the photorefractive grating in the sample.

As with the undoped sample, TPA is the dominant free carrier production mechanism in Fe:SBN:60.

Summary

Single picosecond and subpicosecond light pulses were used in independent experiments to induce refractive index gratings in SBN:60. The time evolution of the gratings appear to have at least two stages which are responsible for two distinct peaks in the FWM signal. The first peak is associated with induced absorption at the probe wavelength. In a single beam experiment, where no grating was present, it was shown that significant probe beam depletion is seen following intense excitation. This depletion is explained as induced absorption due to the population of an impurity or defect site and was associated with the first peak in the FWM signal because the time scales of the two phenomena overlapped. The second peak is explained as resulting from a grating due to a charge displacement photorefractive effect. It can only be observed when the beam geometry is such that photorefractive effects are possible. The TPA coefficient of both samples was measured and the numerical values obtained indicate that TPA is the dominant free carrier production mechanism at the intensities used in these experiments.
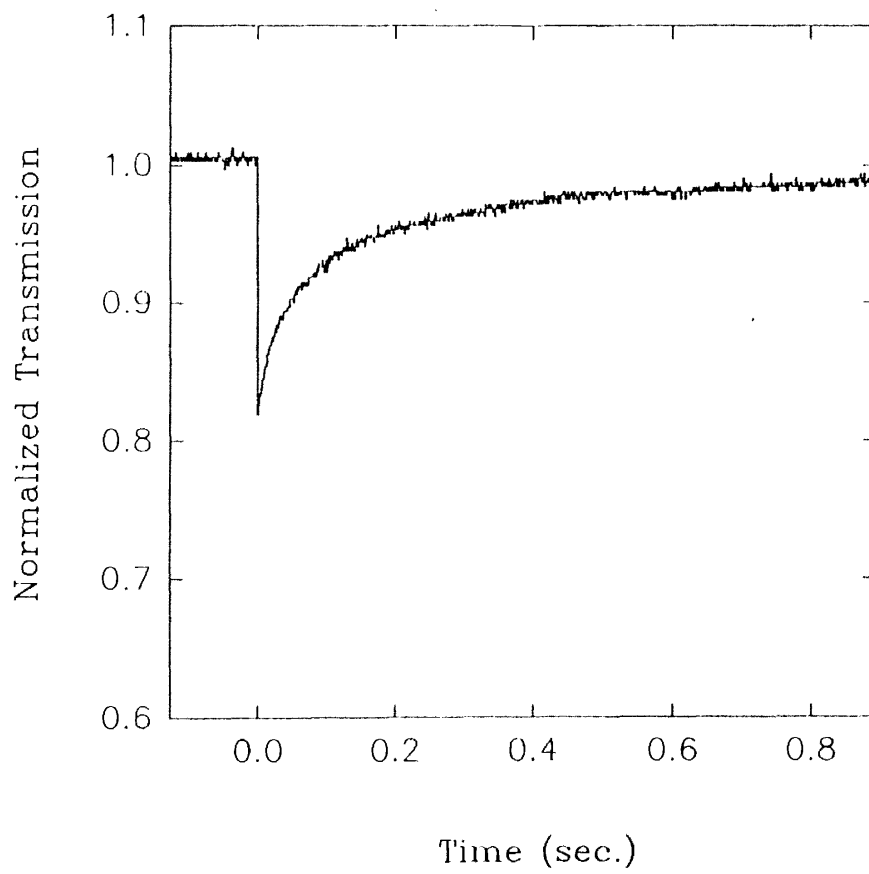
Figure 19. Probe beam depletion following 41.4 microJoule, picosecond excitation.

BIBLIOGRAPHY

1. M. D. Ewbank, R. R. Neurgaonkar, W. K. Cory, and J. Feinberg, J. Appl. Phys. **62**, 374 (1987).

2. D. Rytz, B. A. Wechsler, R. N. Schwartz, C. C. Nelson, C. D. Brandle, A. J. Valentino, and G. W. Berkstresser, J. Appl. Phys. **66**, 1920 (1989).

3. G. Salamo, M. J. Miller, W. W. Clark III, G. L. Wood, and E. J. Sharp, Opt. Comm. **59**, 417 (1986).

4. D. C. Jones and L. Solymar, IEEE J. Quantum Electron. **QE-23**, 372 (1991).

5. J. M. C. Jonathan, G. Roosen, and Ph. Roussignal, Opt. Lett. **13**, 224 (1986).

6. G. Le Saux, G. Roosen, and A. Brun, Opt. Comm. **56**, 374 (1986).

7. J. P. Hermann, J. P. Herriau, J. P. Huignard, App. Opt. **20**, 2173 (1981).

8. J.-L. Ferrier, J. Gazengel, X. N. Phu, and G. Rivoire, Opt. Comm. **58**, 343 (1986).

9. G. Le Saux, J. C. Launay, and A. Brun, Opt. Comm. **57**, 166 (1986).

10. A. Smirl, K. Bohnert, G. C. Valley, R. A. Mullen, and T. Boggess, J. Opt. Soc. Am. **B6**, 606 (1989).

11. L. Lam, T. Y. Chang, J. Feinberg, and R. Hellwarth, Opt. Lett. **6**, 475 (1981).

12. I. Biaggio, M. Zqonik, and P. Gunter, Opt. Comm. **77**, 312 (1990).

13. C.-T. Chen, D. Kin, and D. von der Linde, IEEE J. Quantum Electron. **QE-16**, 126 (1980).

14. R. J. Reeves, H. Liu, and R. C. Powell, To be published Phy. Rev. B.

15. K. Megumi, N. Nagatsuma, K. Kashiwada, and Y. Furuhata, Mater. Sciences **11**, 1583 (1976).

16. P. B. Jamieson, S. C. Abrahams, and J. L. Bernstein, J. Chem. Phys. **48**, 5048 (1968).

17. R. A. Vazquez, M. D. Ewbank, and R. R. Neurgaonkar, Opt. Comm. **80**, 253 (1991).

18. A. Ashkin, G. D. Boyd, J. M. Dziedzik, R. G. Smith, A. A. Ballman, and K. Nassan, Appl. Phys. Lett. **9**, 72 (1966).

19. F. S. Chen, J. T. La Macchia, and D. B. Fraser, Appl. Phys. Lett. **13**, 223 (1968).

20. J. B. Thaxter, Appl. Phys. Lett. **15**, 210 (1969).

21. D. L. Staebler and W. Phillips, Appl. Opt. **13**, 788 (1974).

22. A. M. Glass, D. Von der Linde, and T. J. Negran, Appl. Phys. Lett. **25**, 233 (1974).

23. R. W. Hellwarth, J. Opt. Soc. Am. **67**, 1 (1977).

24. N. V. Kukhtarev, V. B. Markov, S. G. Odulov, and V. L. Vinetskii, Ferro-electrics **22**, 949 (1979).

25. K. Botekjaer, J. Appl. Phys. **48**, 2495 (1977).

26. P. Gunter and J.-P. Huignard, **Photorefractive Materials and Their Applications I** (Springer-Verlag, Berlin, 1988).

27. V. F. Belinicher and B. I. Sturman, Sov. Phys. - Usp. **23**, 199 (1980).

28. S. B. Odulov, JETP Lett. **35**, 10 (1982).

29. M. G. Moharam, T. K. Gaylord, R. Magnusson, J. Appl. Phys. **50**, 5642 (1979).

30. G. C. Valley, IEEE J. of Quant. Electron. **QE-19**, 1637 (1983).

31. M. Goppert-Mayer, Ann. Phys. (Leipz.) **9**, 273 (1931).

32. W. Kaiser and C. G. B. Garrett, Phys. Rev. Lett. **7**, 229 (1961).

33. Y. P. Kim and M. H. R. Huchinson, Appl. Phys. **B49**, 469 (1989).

34. J. H. Bechtel and W. L. Smith, Phys. Rev. **B13**, 3515 (1976).

35. H. J. Eichler, P. Gunter, and D. W. Pohl, **Laser-Induced Dynamic Gratings** (Springer-Verlag, Berlin, 1986).

36. G. Le Saux and A. Brun, IEEE J. of Quant. Electron. **QE-23**, 1080 (1987).

37. A. Yariv, **Quantum Electronics** (John Wiley & Sons, USA, 1989).

38. S. A. Holmstrom, B. Taheri, R. J. Reeves, and R. C. Powell, To be published.

39. S. Ducharme, J. Feinberg, R. R. Neurgaonkar, IEEE J. of Quant. Electron. **QE-23**, 2116 (1987).

40. R. R. Neurgaonkar, W. K. Cory, J. R. Oliver, M. D. Ewbank, and W. F. Hall, Opt. Eng. **26**, 392 (1987).

41. J. F. Nye, **Physical Properties of Crystals** (Oxford Univ. Press, England, 1957).

42. J. B. Thaxter and M. Kestigian, App. Opt. **13**, 913 (1974).

43. J. D. Jackson, **Classical Electrodynamics** (John Wiley & Sons, Singapore, 1990).

VITA 2

SCOTT A. HOLMSTROM

Candidate for the Degree of

Master of Science

Thesis: LASER INDUCED GRATINGS IN STRONTIUM BARIUM NIO-
BATE

Major Field: Physics

Biographical:

Personal Data: Born in St. Louis, Missouri, August 25, 1968, the son of
Richard and Patricia Holmstrom.

Education: Received Bachelor of Science Degree in Physics from Southwest
Missouri State University, Springfield, Missouri, August, 1990; com-
pleted the requirements for the Master of Science degree at Oklahoma
State University, Stillwater, Oklahoma, December, 1993.